CMS Physics Analysis Summary

Contact: cms-pag-conveners-higgs@cern.ch 2017/12/06

Search for additional neutral MSSM Higgs bosons in the di-tau final state in pp collisions at $\sqrt{s} = 13$ TeV

The CMS Collaboration

Abstract

A search is presented for additional neutral Higgs bosons in the di-τ final state in pp collisions at the LHC. The search is performed in the context of the minimal supersymmetric extension of the standard model (MSSM), on the data collected with the CMS detector in 2016 at a center-of-mass energy of 13 TeV, corresponding to an integrated luminosity of 35.9 fb^{-1}. To enhance the sensitivity to neutral MSSM Higgs bosons the search includes the case where the Higgs boson is produced in association with b quarks. No significant deviation above the expected background is observed. Model-independent limits are set on the product of the cross section and branching fraction for the production via gluon-fusion or in association with b quarks. These limits range from 18 pb (at 90 GeV) to 3.5×10^{-3} pb (at 3.2 TeV) for gluon-fusion and from 15 pb (at 90 GeV) to 2.5×10^{-3} pb (at 3.2 TeV) for b-associated production. In the $m_{\mathrm{h}}^{\mathrm{mod+}}$ scenario these limits translate into an exclusion of $\tan\beta > 6$ for $m_{\mathrm{h}} \lesssim 200$ GeV. The exclusion contour ranges up to 1.6 TeV for $\tan\beta < 60$.

1 Introduction

The discovery of a Higgs boson at the CERN LHC in 2012 [1–3] has given evidence that spontaneous symmetry breaking, as proposed by the Brout-Englert-Higgs mechanism [4–9], is indeed realized in nature. The determination of the properties of the new particle, based on the complete LHC Run 1 dataset (2011 and 2012) [10, 11], has revealed its compatibility with the standard model (SM) Higgs boson, within the experimental accuracy. However several questions remain, concerning, for example, the underlying mechanism responsible for the symmetry breaking, or the exact form of the potential that breaks the symmetry. To address these topics one of the main tasks of the LHC is the further exploration of the Higgs sector. One aspect of this is the search for more complex structures, for example, in the form of more than one Higgs doublet. Supersymmetry is an example of a beyond the standard model theory with a more complex Higgs sector [12, 13]. In its minimal implementation, the minimal supersymmetric standard model (MSSM) [14, 15], each particle of the SM is complemented by a supersymmetric partner, which has the same properties apart from its spin. The Higgs sector of the MSSM consists of two complex Higgs doublets, H_u and H_d, to provide masses for *up*- and *down*-type fermions. In the CP-conserving MSSM this leads to the prediction of five physical Higgs particles: two charged Higgs bosons $H^{\pm}$, two neutral scalar Higgs bosons h and H (with $m_h < m_H$) and one neutral pseudoscalar Higgs boson A. At tree-level in the MSSM, the masses of these five Higgs bosons and their mixing can be expressed in terms of the gauge-boson masses and two additional parameters, which can be chosen as the mass of the A boson, m_A, and the ratio of the vacuum expectation values of the neutral components of the two Higgs doublets

$$\tan\beta = \frac{\langle H_u^0 \rangle}{\langle H_d^0 \rangle} = \frac{v_u}{v_d}\,. \tag{1}$$

Dependencies on additional parameters of the soft supersymmetry-breaking mechanism enter via higher order corrections in perturbation theory. In the exploration of the MSSM Higgs sector these parameters are usually set to fixed values in the form of indicative benchmark scenarios [16] to illustrate certain properties of the theory. For values of $m_A \gtrsim 300\,\text{GeV}$, which seem to be favored by data, the MSSM is close to the decoupling limit: the h boson usually takes the role of the observed SM-like Higgs boson at 125 GeV and the H and A bosons are nearly degenerate in mass. At leading order the coupling of the H and the A boson to *down*-type fermions is enhanced with respect to the SM expectation by $\tan\beta$, while the coupling to vector bosons and *up*-type fermions is suppressed by the same amount. The large branching fraction into *down*-type fermions makes searches for additional heavy neutral Higgs bosons that exploit final states containing such fermions particularly interesting. The enhanced coupling to *down*-type fermions also has consequences on the production: Firstly, b-associated production dominates over the production via gluon-fusion for large values of $\tan\beta$. Secondly, in gluon-fusion production the kinematic properties of the Higgs boson change as a function of $\tan\beta$ due to the increasing contribution of b quarks in the fermion loop. Leading order diagrams for H and A production are shown in Fig. 1.

Searches for additional heavy neutral Higgs bosons in the context of the MSSM were carried out in the di-τ final state in e^+e^- collisions at LEP [17] and in $p\bar{p}$ collisions at the Tevatron [18–21] in the past. At the LHC such searches have been carried out by the ATLAS and CMS Collaborations in the b quark [22, 23], di-muon [24, 25] and di-τ [24, 26–30] final states. The better experimental accessibility with respect to the b quark final state and the larger mass, and therefore larger coupling, with respect to the di-muon final state give the di-τ final state a leading role in these searches. In this paper the results of a search for additional heavy neutral

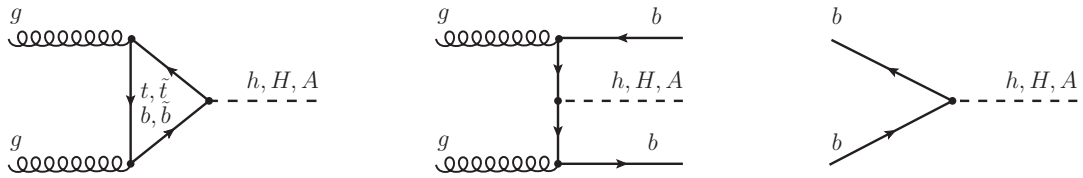

Figure 1: Leading order diagrams for the production of Higgs bosons (left) via gluon-fusion and (middle and right) in association with b quarks. In the middle panel of the figure a pair of b quarks is produced from two gluons (leading order in the four-flavor scheme). In the right panel the Higgs boson is radiated from a b quark in the proton (leading order in the five-flavor scheme).

Higgs bosons in the context of the MSSM are presented. They are based on the full 2016 pp collision dataset from the CMS experiment. These data amount to an integrated luminosity of $\mathcal{L} = 35.9\ \text{fb}^{-1}$. It is the first publication of such a search in the di-τ final state by the CMS Collaboration based on LHC Run 2 data with a center-of-mass energy of 13 TeV. The search makes use of all high-level objects accessible from the reconstructed energy deposits in the detector: electrons, muons, hadronically decaying tau leptons, jets and missing transverse energy. The central element of this analysis is the reconstruction of the di-τ pair. Four different final states are taken into account: eμ, eτ_h, $\mu\tau_\text{h}$ and $\tau_\text{h}\tau_\text{h}$, where τ_h indicates a hadronic τ decay. For this analysis the most significant backgrounds are estimated from data. The techniques that have been used are new with respect to previous publications by CMS. In the absence of signal, upper limits are presented on the product of the cross section and branching fraction for the production of a single narrow resonance via gluon-fusion or in association with b quarks. In addition exclusion contours in the m_A–tan β plane in selected MSSM benchmark scenarios are provided.

2 The CMS detector

The central feature of the CMS apparatus is a superconducting solenoid of 6 m internal diameter, providing a magnetic field of 3.8 T. Within the solenoid volume are a silicon pixel and strip tracker, a lead tungstate crystal electromagnetic calorimeter (ECAL), and a brass and scintillator hadron calorimeter (HCAL), each composed of a barrel and two endcap sections. Forward calorimeters extend the pseudorapidity coverage provided by the barrel and endcap detectors. Muons are detected in gas-ionization chambers embedded in the steel flux-return yoke outside the solenoid.

The silicon tracker measures charged particles within the pseudorapidity range $|\eta| < 2.5$. It consists of 1440 silicon pixel and 15 148 silicon strip detector modules. For nonisolated particles with a transverse momentum of $1 < p_\text{T} < 10\,\text{GeV}$ and $|\eta| < 1.4$, the track resolutions are typically 1.5% in p_T and 25–90 (45–150) μm in the transverse (longitudinal) impact parameter [31]. In the barrel section of the ECAL, an energy resolution of about 1% is achieved for unconverted or late-converting photons in the tens of GeV energy range. The remaining barrel photons have a resolution of better than 2.5% for $|\eta| \leq 1.4$. In the endcaps, the resolution of unconverted or late-converting photons is about 2.5%, while the remaining endcap photons have a resolution between 3% and 4% [32]. For electrons from Z boson decays, the momentum resolution varies from 1.7%, for well-measured electrons in the barrel, to 4.5% for electrons, which e.g., loose a significant amount of their energy through bremsstrahlung, in the endcap [33]. When combining information from the entire detector, the jet energy resolution amounts typi-

cally to 15% at 10 GeV, 8% at 100 GeV, and 4% at 1 TeV, to be compared to about 40%, 12%, and 5% obtained when the ECAL and HCAL calorimeters alone are used. Muons are measured in the pseudorapidity range $|\eta| < 2.4$, with detection planes made using three technologies: drift tubes, cathode strip chambers, and resistive plate chambers. Matching muons to tracks measured in the silicon tracker results in a relative transverse momentum resolution for muons with $20 < p_{\mathrm{T}} < 100$ GeV of 1.3–2.0% in the barrel and better than 6% in the endcaps. The p_{T} resolution in the barrel is better than 10% for muons with p_{T} up to 1 TeV [34].

Events of interest are selected using a two-tiered trigger system [35]. The first level (L1), composed of custom hardware processors, uses information from the calorimeters and muon detectors to select events at a rate of around 100 kHz within a time interval of less than 4 μs. The second level, known as the high-level trigger (HLT), consists of a farm of processors running a version of the full event reconstruction software optimized for fast processing, and reduces the event rate to around 1.2 kHz before data storage.

A more detailed description of the CMS detector, together with a definition of the coordinate system used and the relevant kinematic variables, can be found in Ref. [36].

3 Event reconstruction

The reconstruction of the proton-proton collision products is based on the particle-flow (PF) algorithm as described in Ref. [37], combining the available information from all CMS subdetectors to reconstruct an unambiguous set of individual particle candidates. These particle candidates are categorized into muons, electrons, photons and charged and neutral hadrons. During the 2016 data taking period the CMS experiment was operating with, on average, 23 proton-proton collisions per bunch crossing. A fully recorded proton-proton collision defines an *event* for further processing. Collision vertices are obtained from reconstructed tracks using a deterministic annealing algorithm [38]. The *primary collision vertex*, presumed to contain the hard interaction of interest, is taken as the reconstructed vertex with the largest value of the sum of the p_{T}^2 of all tracks associated with it. Any other vertices in the event are associated with additional soft inelastic proton-proton collisions called *pileup*.

Muons in the event are reconstructed by performing a simultaneous track fit to hits in the tracker and in the muon chambers [34]. The presence of hits in the muon chambers already leads to a strong suppression of particles misidentified as muons. Additional identification requirements on the track fit quality and the compatibility of individual track segments with the fitted track can reduce the misidentification rate further. For this analysis muon identification requirements with an efficiency of $\approx$99% are chosen. Electrons are reconstructed by combining clusters of energy deposits in the ECAL with hits in the tracker [33]. To increase their purity, reconstructed electrons are required to pass a multivariate electron identification discriminant, which combines information on track quality, shower shape and kinematic quantities [39]. For this analysis working points with an efficiency between 80% and 90% are used to identify electrons. The contribution from backgrounds to the electron (muon) selection is further reduced by requiring the corresponding lepton to be isolated from any other hadronic activity in the detector. This property is quantified by a relative isolation variable $I_{\mathrm{rel}}^{e(\mu)}$, which starts from the sum of the transverse momentum (energy) of all charged (neutral) particles, $I_{\mathrm{abs}}^{e(\mu)} = (\sum p_{T,i} + \sum E_{T,i})$. The lepton itself is not included in this calculation. From all other particles only those in a predefined cone of radius $\Delta R = \sqrt{\Delta\eta^2 + \Delta\phi^2}$ around the lepton direction at the primary collision vertex are taken into account, where $\Delta\eta$ and $\Delta\phi$ correspond to the angular distance of the particle to the lepton in the η and ϕ directions. The chosen cone

size is $\Delta R < 0.4\,(0.3)$ for muons (electrons). To mitigate any distortions from pileup only those charged particles whose tracks are associated with the primary collision vertex are taken into account. The presence of neutral particles from pileup is estimated by summing the transverse momenta of charged particles in the isolation cone whose tracks have been associated to pileup vertices, and multiplying this quantity by a factor of 0.5 to account for the approximate ratio of neutral to charged hadron production. The value obtained is subtracted from $I_{\text{abs}}^{e(\mu)}$, while the minimum value is fixed to zero. Finally the result obtained is divided by the p_{T} of the lepton.

For further characterization of the event all reconstructed PF objects are clustered into jets using the anti-k_{T} jet clustering algorithm as implemented in FASTJET [40] with a distance parameter of 0.4. To identify jets resulting from the hadronization of b quarks the *combined secondary vertex* b-tagging algorithm as described in Ref. [41] is used, which exploits information from the decay vertices of long-lived mesons, and the impact parameters of charged particle tracks, in a combined discriminant. In this analysis a working point corresponding to a b-jet identification efficiency of ≈70% and a misidentification rate for light quarks and gluons of 1% has been chosen. Jets are also used as seeds for the reconstruction of hadronic τ decays. This is done by further exploiting the substructure of the jets, using the *hadron-plus-strips* algorithm, as described in Refs. [42, 43]. For the analysis the decay into three charged hadrons and the decay into one single charged hadron accompanied by up to two neutral pions with $p_T > 2.5\,\text{GeV}$ are used. The neutral pions are reconstructed as *strips* with dynamic size from reconstructed electrons and photons contained in the seeding jet, where the strip size varies as a function of the p_{T} of the electron or photon candidate. The τ_h decay mode is then obtained by combining the charged hadrons with the strips. As particles without color charge, high p_{T} tau leptons are expected to be isolated from all hadronic activity in the event as are high p_{T} muons and electrons. Furthermore in accordance with its finite lifetime the charged decay products of the τ lepton are expected to be slightly displaced from the primary collision vertex. To distinguish hadronic τ decays from jets originating from the hadronization of quarks or gluons a multivariate τ_h-identification discriminant is used [42]. It combines information on the hadronic activity in the detector in the vicinity of the τ_h candidate with the reconstructed lifetime information from the tracks of the charged decay products. Of the predefined working points this analysis makes use of the `Tight`, `Medium` and `VeryLoose` working points. These have efficiencies of 27% (`Tight`), 51% (`Medium`) and 71% (`VeryLoose`), for quark/gluon misidentification rates of less then 4.4×10^{-4} (`Tight`), 3.3×10^{-3} (`Medium`) and 1.3×10^{-2} (`VeryLoose`). Finally requirements are imposed to reduce the misidentification of electrons and muons as τ_h. Also here predefined working points are used to discriminate against electrons, with efficiencies ranging from 65% (`Tight`) to 94% (`VeryLoose`) for electron misidentification rates between 6.2×10^{-4} (`Tight`) and 2.4×10^{-2} (`VeryLoose`). The misidentification rate of muons as τ_h is of $\mathcal{O}(10^{-3})$, for a signal efficiency of 99%.

The missing transverse momentum vector $\vec{p}_T^{\,\text{miss}}$, defined as the negative vector sum of the transverse momenta of all reconstructed PF objects, is also used to characterize the events. Its magnitude is referred to as E_T^{miss}. It is used for the discrimination of backgrounds that are expected to contain neutrinos with significant transverse momentum such as W boson production in association with jets (W+jets). It is furthermore used for the calculation of the final discriminating variable that is used for the statistical inference of the signal, as detailed in Section 6.

4 Event selection and categorization

The four most sensitive final states of the di-τ pair are exploited: eμ, eτ_h, $\mu\tau_h$, and $\tau_h\tau_h$. The online selection for the eτ_h ($\mu\tau_h$) final state is based on the presence of at least one electron (muon) with $p_T > 25\,(22)$ GeV at trigger level. In addition, triggers with a restriction of $|\eta| < 2.1$ for the corresponding lepton are used. The online selection for the eμ final state relies on a logical *or* of two lower threshold triggers that both require the presence of an electron and muon in the event with $p_T > 23$ GeV for the higher p_T lepton and $p_T > 12\,(8)$ GeV for the lower p_T electron (muon). In the $\tau_h\tau_h$ final state, a trigger decision based on the presence of two hadronically decaying tau leptons with $p_T > 35$ GeV and $|\eta| < 2.1$ is used. In addition to the trigger selection, requirements on the p_T and η of the reconstructed τ decay products are applied in the offline analysis as given in Table 1.

Table 1: Kinematic selection of the final state objects in the eμ, eτ_h, $\mu\tau_h$ and $\tau_h\tau_h$ final state. The expression "first (second) lepton" refers to the channel label used in the first column.

final state	first lepton	second lepton
$e\mu^{(1)}$	p_T^e>13 GeV, $\|\eta^e\|$<2.5	p_T^μ >10 GeV, $\|\eta^\mu\|$<2.4
eτ_h	p_T^e>26 GeV, $\|\eta^e\|$<2.1	$p_T^{\tau_h}$>30 GeV, $\|\eta^{\tau_h}\|$<2.3
$\mu\tau_h$	p_T^μ>23 GeV, $\|\eta^\mu\|$<2.1	$p_T^{\tau_h}$>30 GeV, $\|\eta^{\tau_h}\|$<2.3
$\tau_h\tau_h$	$p_T^{\tau_h} > 40$ GeV, $\|\eta^{\tau_h}\| < 2.1$	

(1) $p_T > 24$ GeV on the higher p_T trigger match (see text).

In the eμ final state an electron with $p_T > 13$ GeV and $|\eta| < 2.5$ and a muon with $p_T > 10$ GeV and $|\eta| < 2.4$ are required. In the case that the event passed only one trigger path the lepton identified with the higher p_T trigger object is required to have a $p_T > 24$ GeV. Both leptons are required to pass identification criteria as described in Section 3 and to be isolated according to $I_{\text{rel}}^{e(\mu)} < 0.15\,(0.2)$. Events with additional leptons fulfilling looser selection requirements than these are rejected from the analysis. In the eτ_h ($\mu\tau_h$) final state an electron (muon) with $p_T > 26\,(23)$ GeV and $|\eta| < 2.1$ and a τ_h candidate with $p_T > 30$ GeV and $|\eta| < 2.3$ is required. The electron (muon) and the τ_h candidate should fulfill the identification requirements described in Section 3. The τ_h candidate should pass the `Tight` working point of the τ_h-identification discriminant, the `Tight` (`VeryLoose`) working point of the anti-electron discriminant and the `Loose` (`Tight`) working point of the anti-muon discriminant in the eτ_h ($\mu\tau_h$) case. In addition the electron (muon) should be isolated according to $I_{\text{rel}}^{e(\mu)} < 0.1\,(0.15)$. Events with additional leptons fulfilling looser selection requirements are rejected from the analysis. In the $\tau_h\tau_h$ final state two τ_h candidates with $p_T > 40$ GeV and $|\eta| < 2.1$ are required. Both are required to pass the `Medium` working point of the τ_h-identification discriminant, the `VeryLoose` working point of the discriminant against electrons and the `Loose` working point of the discriminant against muons. Events with additional electrons or muons fulfilling looser requirements on identification, isolation and p_T than described for the eτ_h or $\mu\tau_h$ final state above are rejected from the analysis.

In all cases the final state products are required to be of opposite charge, to be separated by more than 0.5 in ΔR and to be associated to the primary collision vertex within a distance of $d_{xy} < 0.045$ cm in the transverse plane for electrons and muons and $d_z < 0.2$ cm along the beam axis for all final state objects. The vetoes of additional leptons help with the suppression of backgrounds and ensure that no event will be categorized according to more than one di-τ final state. In at most 0.8% of the selected events are there multiple τ_h candidates. In this case, the di-τ pair with the most isolated final state products is chosen.

To increase the sensitivity of the analysis all selected events are further categorized: in all final states events with at least one jet with $p_T > 20\,\text{GeV}$ and $|\eta| < 2.4$ that passes the b-tagging requirement described in Section 3 are associated to a global `B-tag` category. This category is designed to target the b-associated production of the Higgs boson. All other events are associated to a global `No B-tag` category.

In the $e\mu$ final state each global event category is further split into three sub-categories based on the quantity D_ζ defined as

$$D_\zeta = p_\zeta^{\text{miss}} - 0.85\, p_\zeta^{\text{vis}} \quad ; \quad p_\zeta^{\text{miss}} = \vec{p}_T^{\,\text{miss}} \cdot \hat{\zeta} \quad ; \quad p_\zeta^{\text{vis}} = \left(\vec{p}_T^{\,e} + \vec{p}_T^{\,\mu}\right) \cdot \hat{\zeta}\,, \tag{2}$$

where $\vec{p}_T^{\,e(\mu)}$ corresponds to the transverse momentum vector of the electron (muon) and $\hat{\zeta}$ to the bisectional direction between the electron and the muon in the transverse plane. The categories are defined as `Low-`D_ζ ($-50 < D_\zeta \leq -10\,\text{GeV}$), `Medium-`$D_\zeta$ ($-10 < D_\zeta \leq 30\,\text{GeV}$) and `High-`$D_\zeta$ ($D_\zeta > 30\,\text{GeV}$). In this way categories with different signal purities and $\bar{\text{t}}\text{t}$ fractions can be exploited during the statistical inference for the signal. The expected signal, for all masses tested, is mostly located in the `Medium-`D_ζ sub-category.

In the $e\tau_h$ ($\mu\tau_h$) final state each global event category is further split into two sub-categories based on the transverse mass

$$m_T^{e(\mu)} = \sqrt{2\, p_T^{e(\mu)}\, E_T^{\text{miss}}\, (1 - \cos\Delta\phi)}\,, \tag{3}$$

where $p_T^{e(\mu)}$ refers to the p_T of the electron (muon) and $\Delta\phi$ to the azimuthal angle in the transverse plane between the electron (muon) and $\vec{p}_T^{\,\text{miss}}$. The categories are defined as `Tight-`m_T ($m_T^{e(\mu)} < 40\,\text{GeV}$) and `Loose-`$m_T$ ($40 < m_T^{e(\mu)} < 70\,\text{GeV}$). The bulk of the signal events, particularly for low mass hypotheses, lie in the `Tight-`m_T sub-category. The `Loose-`m_T category has been added to increase the signal acceptance for mass hypotheses of $m_{\text{A,H}} > 700\,\text{GeV}$.

In combination this leads to 16 event categories entering the signal inference, complemented by three background control regions, as discussed in Section 5. In Fig. 2, the D_ζ and m_T^μ distribution are shown in the $e\mu$ and $\mu\tau_h$ final states respectively, before splitting the events into categories, indicating the corresponding sub-categorization. A description of the exact composition of the background is given in Section 6. A graphical representation of the complete event categorization is given in Fig. 3.

5 Event simulation and background estimation

A list of all SM backgrounds that contribute to the event selection described in Section 4 is given in Table 2. The most obvious background originates from Z boson production in the di-τ final state ($\text{Z} \to \tau\tau$). Since the analysis is not sensitive to the CP-eigenvalue or spin of the Higgs boson the signal can be distinguished from this background only by the difference in mass of the associated bosons. The same is true for $\text{Z} \to \ell\ell$ events, where ℓ refers to an electron or muon, if one of the leptons is misidentified as τ_h. Similar arguments hold for $\bar{\text{t}}\text{t}$ production, which is a dominant background especially in the $e\mu$ final state, the production of single top quarks and vector boson pair production (WW, WZ and ZZ). Common to all these backgrounds in the $e\tau_h$, $\mu\tau_h$ and $\tau_h\tau_h$ final states is that they can be misinterpreted as signal events in two ways: Firstly, if the final state contains one or more genuine tau leptons or if an electron or muon in

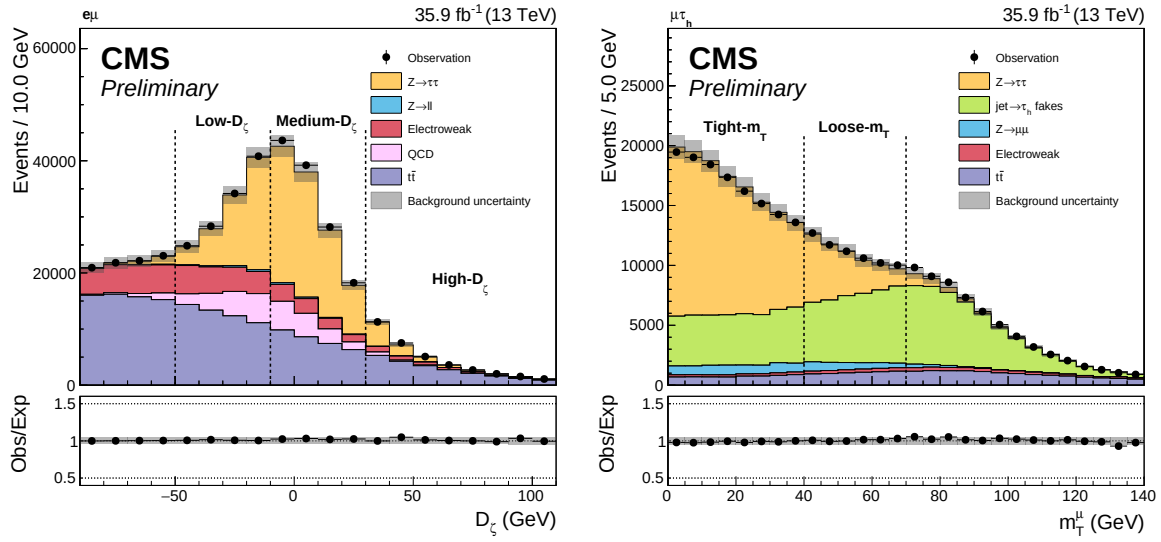

Figure 2: Observed and expected distributions of (left) D_ζ in the eμ final state and (right) m_T^μ in the $\mu\tau_\mathrm{h}$ final state. The vertical lines in the figures indicate the definition of the sub-categories in each final state. The distributions are shown before any event categorization and prior to the fit used for the statistical inference of the signal. For these figures no uncertainties that effect the shape of the distributions have been included in the uncertainty model.

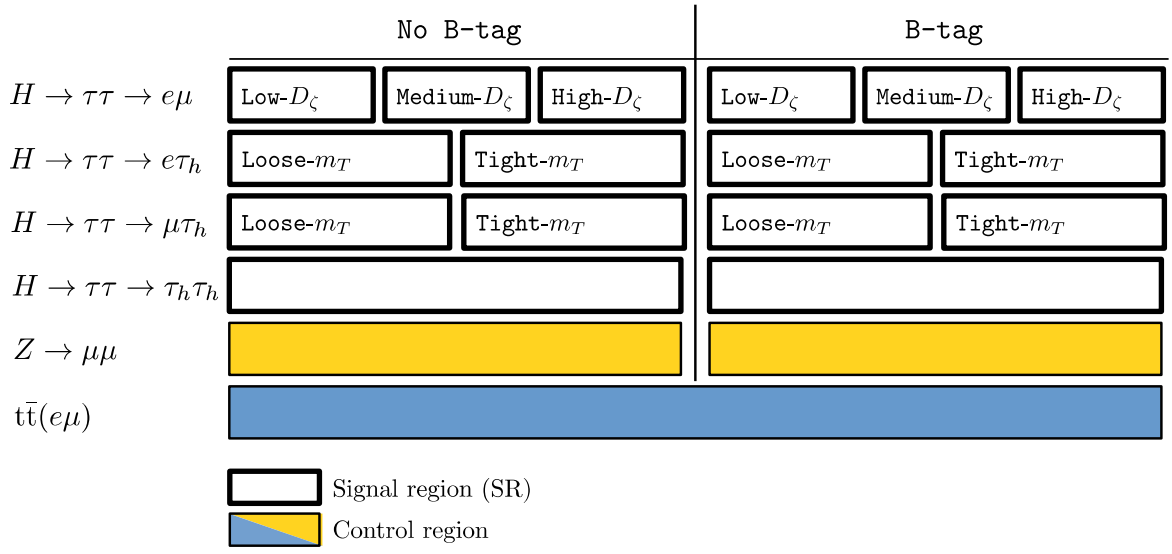

Figure 3: Overview of all event sub-categories that enter the statistical inference of the signal in the analysis. Sixteen signal categories are complemented by three background control regions in the main analysis as described in Section 5.

the final state is misinterpreted as τ_h. In Table 2 these processes are labeled by "$\tau/\ell \to \tau_h$". Secondly, if only one electron or muon in the final state is identified and a jet is misinterpreted as τ_h. In Table 2 these processes are labeled by "jet $\to \tau_h$". Backgrounds due to W+jets or due to SM events comprised uniquely of jets produced through the strong interaction, referred to as quantum chromodynamics (QCD) multijet production, predominantly contribute to the event selection via the misidentification of jets as τ_h. The level to which each of these processes contributes to the event selection depends on the final state.

5.1 Event simulation

Drell-Yan events in the di-electron, di-muon and di-τ final state and W+jets events have been generated at leading-order (LO) $2 \to N$ precision in the coupling strength α_s using the MADGRAPH 5 event generator [44]. To increase the number of simulated events in regions of high signal purity additional samples have been generated with different numbers of outgoing partons in the hard interaction. For diboson production MADGRAPH 5_AMC@NLO has been used [45] at next-to-leading order (NLO) precision. For $t\bar{t}$ and single top quark production samples have been generated at NLO precision using POWHEG [46–51]. For the interpretation of the results the expected contribution of the SM Higgs boson is taken into account; this process has been simulated using POWHEG separately for the production via gluon-fusion, vector boson fusion (VBF) or in association with a Z (ZH) or W boson (WH). When compared to data and not modified by a control measurement in data, Drell-Yan, W+jets, $t\bar{t}$ and single top quark events in the tW-channel are normalized to their cross sections at next-to-next-to-leading order (NNLO) precision [52]. Single top quark production in the t-channel [53] and di-boson events are normalized to their cross sections at NLO precision [54].

The gluon-fusion signal process has been simulated at LO precision using PYTHIA 8.212 [55]. For the statistical inference of the signal the Higgs boson p_T distribution is weighted to NLO precision using POWHEG. To account for the multiscale nature of the process in the NLO plus parton shower POWHEG prediction, the p_T spectra corresponding to the contributions from the t quark alone, the b quark alone and the tb-interference are each calculated separately, using a POWHEG damping factor set to the individual scales as discussed in Refs. [56–58]. For the model-independent limits the individual distributions are combined according to their contribution to the total cross section as expected for a CP-even Higgs boson with given mass in the SM. In the model-dependent interpretation in the MSSM, where the contribution from each individual distribution in addition depends on the model parameters, these contributions are obtained using POWHEG in the two Higgs doublet mode. Each distribution is scaled, depending on the model parameters, using the effective Yukawa couplings as predicted by the corresponding benchmark model, before all distributions are combined into one single prediction. In this context also the $\tan\beta$ enhanced supersymmetric corrections to the b quark coupling in the $m_h^{\text{mod+}}$ scenario are taken into account via the corresponding effective Yukawa coupling. Other supersymmetric contributions are neglected by this procedure. These contributions have been checked to be less than a few percent. The b-associated production has been simulated at NLO precision using MADGRAPH 5_AMC@NLO.

For the generation of all processes the NNPDF3.0 parton distribution functions have been used as described in Ref. [59]. The description of the underlying event has been parametrized according to the CUETP8M1 tune as described in Ref. [60]. Hadronic showering and hadronization, as well as the τ decays, have been modeled using PYTHIA. For all simulated events the effect of the observed pileup has been taken into account. For this purpose additional inclusive inelastic pp collisions have been generated with PYTHIA and added to all simulated events according to the expected pileup profile. All events generated have been passed through a

GEANT [61] based simulation of the CMS detector and reconstructed using the same version of the CMS event reconstruction software as used for the data.

Table 2: Background processes contributing to the event selection as given in Section 4. The further splitting of the processes in the second column refers only to final states with a τ_h candidate. MC implies that the process is taken from simulation, FF implies that the process is determined from data using fake factors as described in the text. The symbol CR implies that both the shape and normalization of QCD multijet events are estimated from control regions in data. The label ℓ corresponds to an electron or muon.

background process	misidentification	$e\mu$	$e\tau_h$	$\mu\tau_h$	$\tau_h\tau_h$
$Z \to \tau\tau$		MC†	MC†	MC†	MC†
$Z \to \ell\ell$	$\ell \to \tau_h$	MC	MC	MC	MC
	jet $\to \tau_h$		FF	FF	FF
Diboson+single top	$\tau/\ell \to \tau_h$	MC	MC	MC	MC
	jet $\to \tau_h$		FF	FF	FF
$t\bar{t}$	$\tau/\ell \to \tau_h$	MC†	MC†	MC†	MC†
	jet $\to \tau_h$		FF	FF	FF
W+jets	jet $\to \tau_h$	MC	FF	FF	FF
QCD	jet $\to \tau_h$	CR	FF	FF	FF

† Normalization from control region in data.

5.2 Backgrounds estimated from data

As outlined in Table 2 a large fraction of the backgrounds in the $e\tau_h$, $\mu\tau_h$ and $\tau_h\tau_h$ final states can be attributed to jets misidentified as τ_h. For the statistical inference of the signal the shape and normalization of these backgrounds are estimated from control regions in data, using the *fake factor* method. In this approach the estimated number of events for a certain background i due to jet $\to \tau_h$-misidentification is estimated from a region that only differs from the *signal region* (SR) by modifying the τ_h-identification requirement. This region is referred to as the *application region* (AR). For this purpose the τ_h-identification is required to fulfill the `VeryLoose` but not the `Tight` (`Medium`) working point of the discriminant in the $e\tau_h/\mu\tau_h$ ($\tau_h\tau_h$) final state. This region is primarily populated by events with jets misidentified as τ_h, with typical impurities from genuine τ_h decays at the level of a few percent or below. To arrive at an estimate for the number of events from background i due to jet $\to \tau_h$-misidentification in the SR the number of events in the AR is then multiplied by the ratio

$$\mathrm{FF}_i = \frac{n_{\texttt{Tight/Medium}}}{n^{\texttt{VeryLoose}}_{\texttt{!Tight/Medium}}}, \tag{4}$$

where $n_{\texttt{Tight/Medium}}$ corresponds to the number of events that fulfill the `Tight/Medium` working point and $n^{\texttt{VeryLoose}}_{\texttt{!Tight/Medium}}$ to the number of events that fulfill the `VeryLoose` but not the `Tight/Medium` working point of the τ_h-identification discriminant. The inputs to Eq. (4) are obtained from a dedicated *determination region* (DR_i), which is dominated by background i. To remove contributions from backgrounds other than i, those are estimated from simulation and subtracted from the numerator and denominator of Eq. (4). The ratio FF_i is referred to as the

fake factor for background i throughout the text. The underlying assumption in this method is that the fake factor is the same in the AR and the DR_i. This can be ensured by determining FF_i differentially as a function of several variables. Residual biases can be removed by adequate corrections, which can be determined from control regions or from the simulation. For the analysis the fake factor has been estimated as a function of the p_T of the τ_h candidate in categories of the τ_h decay mode, and the jet multiplicity, in bins of $N_{jet} = 0$ or $N_{jet} \geq 1$. This has been done independently in dedicated determination regions, DR_i, for the backgrounds due to QCD multijet, W+jets and $\mathrm{t\bar{t}}$ events.

For the $\mathrm{e}\tau_\mathrm{h}$ and $\mu\tau_\mathrm{h}$ final states DR_QCD is defined by the same selection as for the SR, but the electric charges of the di-τ pair are required to be of the same sign. To reduce the contamination from W+jets events the transverse mass is required to be $m_T^{e(\mu)} < 40\,\mathrm{GeV}$. Finally the relative isolation requirement on the electron (muon) is changed to $0.05 < I_\mathrm{rel}^{e(\mu)} < 0.15$ in both final states. The definition of $\mathrm{DR}_\mathrm{W+jets}$ also uses the same selection as for the SR, but the requirement on the transverse mass is changed to $m_T^{e(\mu)} > 70\,\mathrm{GeV}$ to enrich this background and an additional requirement of the absence of b jets in the event is imposed to reduce the contamination from $\mathrm{t\bar{t}}$ events. In the $\mathrm{e}\tau_\mathrm{h}$ and $\mu\tau_\mathrm{h}$ final states $\mathrm{t\bar{t}}$ production is a sub-dominant background with respect to W+jets and QCD multijet events. Since there is no sufficiently populated pure DR for $\mathrm{t\bar{t}}$ events covering a similar phase space as the SR, the fake factors for $\mathrm{t\bar{t}}$ events in this case are estimated from simulation after the event selection and before the event categorization. Corrections to these fake factors have been derived from a dedicated control region as described below. In the $\tau_\mathrm{h}\tau_\mathrm{h}$ final state, DR_QCD is obtained from the single requirement that the electric charges of the di-τ pair should be of same sign. As, for this final state, QCD multijet production is by far the dominant background, the fake factors measured in DR_QCD are also used to estimate the background from W+jets and $\mathrm{t\bar{t}}$ events. In the $\mathrm{e}\tau_\mathrm{h}$ and $\mu\tau_\mathrm{h}$ final states a weighted fake factor FF is obtained on an event-by-event basis from

$$\mathrm{FF} = \sum_i w_i \cdot \mathrm{FF}_i \quad , \quad w_i = \frac{N_\mathrm{AR}^i}{\sum_j N_\mathrm{AR}^j} \quad , \quad i \in \{\mathrm{QCD}, \mathrm{W+jets}, \mathrm{t\bar{t}}\}\,, \tag{5}$$

where N_AR^i corresponds to the expected number of events for background i in the AR. The weighted fake factor is then applied to all events in the AR to obtain an estimate for the number and shape of the sum of QCD multijet, W+jets and $\mathrm{t\bar{t}}$ events due to jet $\rightarrow \tau_h$-misidentification. For this purpose the sub-dominant contributions from $\mathrm{Z} \rightarrow \ell\ell$, diboson and single top quark events are subsumed into the W+jets estimate. From the resulting distributions, the expected contribution from events with genuine τ_h decays or misidentified electrons or muons are subtracted using the simulation. In the $\tau_\mathrm{h}\tau_\mathrm{h}$ final state, where each of the τ_h decays usually originates from jet $\rightarrow \tau_h$-misidentification each event enters the AR twice, either if the leading τ_h candidate fulfills the nominal τ_h-identification requirement and the sub-leading τ_h candidate the inverted requirement or vice versa. In each case a weight of 0.5 is applied to take the combinatorial effect into account. For the backgrounds from W+jets and $\mathrm{t\bar{t}}$ events typically one of the reconstructed τ_h candidates originates from a genuine τ lepton, while the other one is due to a misidentified jet. The fraction of events with two misidentified jets is at most a few percent and thus well below the associated systematic uncertainties. Since there are no significant combinatorial effects involved these events are taken into account with a weight of 1.

For the determination of FF the expected contribution from W+jets, $\mathrm{Z} \rightarrow \ell\ell$, diboson, single top quark and $\mathrm{t\bar{t}}$ events to the AR is estimated from simulation. The expected contribution

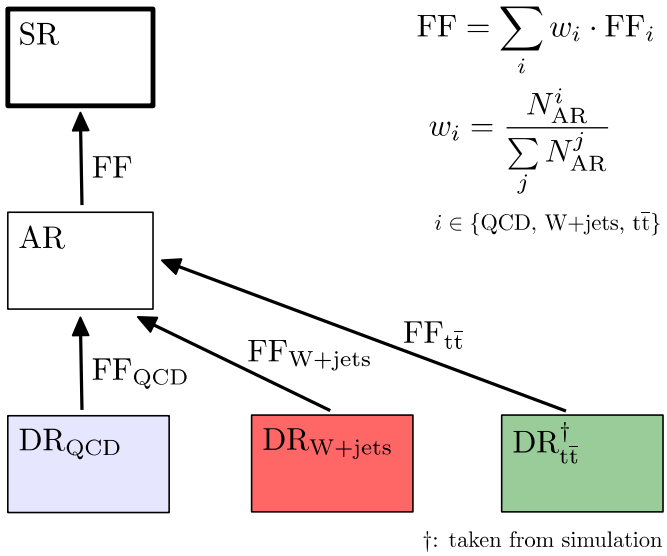

Figure 4: Schematic view of the determination and application of fake factors for the estimation of the background from QCD multijet, W+jets and $\mathrm{t\bar{t}}$ events due to the misidentification of jets as τ_h. Note that $\mathrm{DR}^{\dagger}_{\mathrm{t\bar{t}}}$ is taken from simulation.

from QCD multijet events is estimated from the events in the AR after subtracting all other backgrounds. This estimate has been cross checked using a template fit to the data in the AR similar to the fit described in Section 6 for the statistical inference of the signal, but with the $p_{\mathrm{T}}(\tau_h)$ distribution as the input shape. The principle of the method is outlined in Fig. 4.

For each of the backgrounds considered corrections to the estimated fake factors are determined in dedicated control regions to account for residual biases of the method. These may originate from the finite number of events or the functional form of the fit with which the FF_i have been derived and from sub-dominant dependencies that have been neglected during the fake factor determination. These effects are checked and corrected for in the DR_i themselves by comparing the actual number of events with the τ_h decay matching the `Tight/Medium` working point of the τ_h-identification discriminant to the number of events estimated from the method. Residual corrections have been determined as a function of the invariant mass of the visible decay products of the di-τ pair, m_{vis}, and found to be compatible with unity within the statistical precision. This demonstrates that the main dependencies of the FF_i have been taken into account. For $\mathrm{FF}_{\mathrm{QCD}}$ two additional corrections are applied: In the $\mathrm{e}\tau_{\mathrm{h}}$ ($\mu\tau_{\mathrm{h}}$) final state a correction is obtained as a function of $I^{e(\mu)}_{\mathrm{rel}}$ by comparing the number of events matching the `Tight/Medium` working point of the τ_h-identification discriminant to the number of events estimated from the method in a control region equivalent to $\mathrm{DR}_{\mathrm{QCD}}$, with the only difference that the initial requirement on $I^{e(\mu)}_{\mathrm{rel}}$ has been dropped. This correction has been found to be $\mathcal{O}(10\%)$ and compatible with unity within one standard deviation of the statistical precision. In the $\tau_{\mathrm{h}}\tau_{\mathrm{h}}$ final state a similar correction is derived as a function of the p_{T} of the other τ_h candidate. This correction has been found to range between a few percent and 20%.

For all final states another correction is derived to account for the transition from $\mathrm{DR}_{\mathrm{QCD}}$ with the same charge requirement on the di-τ pair to the SR with an opposite charge requirement. This correction is determined as a function of m_{vis} in a control region with $0.1 < I^{e}_{\mathrm{rel}} < 0.2$ ($0.15 < I^{\mu}_{\mathrm{rel}} < 0.25$) in the $\mathrm{e}\tau_{\mathrm{h}}$ ($\mu\tau_{\mathrm{h}}$) final state and in a control region where the other τ_h candidate matches the `VeryLoose` but fails the `Medium` working point of the τ_h-identification

discriminant in the $\tau_h\tau_h$ final state. In all final states the correction has been found to be compatible with unity within one standard deviation of the statistical precision, which ranges from 10% to 20% in the $e\tau_h$ and $\mu\tau_h$ final states and from a few percent to 10% in the $\tau_h\tau_h$ final state. In the $e\tau_h$ ($\mu\tau_h$) final state a correction is derived from simulation for FF_{W+jets} as a function of $m_T^{e(\mu)}$. A residual dependency is expected from the selection requirements on $p_T^{e(\mu)}$: For low $m_T^{e(\mu)}$ a value of $p_T^{e(\mu)}$ above the thresholds of the offline selection will lead to a harder hadronic recoil and more jets in the event. This in turn may lead to less isolated τ_h candidates especially at low $p_T(\tau_h)$. The correction ranges from 10% to 30%, while usually compatible with unity within one standard deviation of the statistical precision. This correction is assumed to be the same for $Z \to \ell\ell$, diboson and single top quark events. The fake factors for $t\bar{t}$ events, $FF_{t\bar{t}}$, are obtained from simulation and corrections are derived from a control region in data. This control region is characterized by the presence of at least one b jet and at least one lepton pair consisting of an isolated electron and an isolated muon in the event. Since this correction has been found to have no obvious differential dependencies within the experimental precision a common factor is used depending on the final state ($e\tau_h$ or $\mu\tau_h$) and the τ_h decay mode.

In the $e\mu$ final state the background from QCD multijet events is estimated from an AR fulfilling the same selection requirements as the SR, however the charges of the leptons are required to be of the same sign. Extrapolation factors for the same-sign to the opposite-sign phase space are obtained in bins of the p_T of the two leptons and their separation in ΔR. These extrapolation factors are derived in a DR region without event categorization, in which the isolation requirements on the leptons are chosen to be orthogonal to the SR. Finally corrections are applied to account for the extrapolation into the exclusive event categories and for the extrapolation into the SR. The corrections for the extrapolation into the exclusive event categories are determined from the same DR, but inclusive in the p_T of, and separation between, the leptons. They are about 0.6 (1) for all `B-tag` (`No B-tag`) categories. The correction for the extrapolation into the SR is about 0.9 as determined from simulation.

5.3 Backgrounds estimated from simulation

All other backgrounds are taken from simulation. For this purpose the simulated events are corrected to match the pileup distribution observed in data. Further corrections are derived to account for residual differences in the efficiency of the selected trigger paths, for the differences in the electron and muon tracking efficiency and in the efficiency of the identification and isolation requirements for electrons and muons. These corrections are obtained using the tag-and-probe method as described in Ref. [62] with $Z \to ee$ and $Z \to \mu\mu$ events in bins of p_T and η. They are usually not larger than a few percent. In a similar way, corrections are obtained for the efficiency of triggering the τ_h decays in the $\tau_h\tau_h$ final state and for the τ_h-identification efficiency. In this case the tag-and-probe method is applied to $Z \to \tau\tau$ events in the $\mu\tau_h$ final state.

The energies of jets are corrected to the expected response of the jet at stable hadron level, using corrections measured in bins of the jet p_T and η. These corrections are usually not larger than 10–15%. Residual data-to-simulation corrections are applied to the simulated samples. They usually range between sub-percent level at high jet p_T in the central part of the detector to a few percent in the forward region. A correction is applied to the direction and magnitude of the $\vec{p}_T^{\,\text{miss}}$ vector based on differences between estimates of the hadronic recoil in $Z \to \mu\mu$ events in data and simulation. This correction is applied to $Z \to \tau\tau$, W+jets and signal events, where a well defined direction and magnitude of genuine $\vec{p}_T^{\,\text{miss}}$ can be defined. The efficiency for real and misidentified b jets to pass the `Medium` working point of the b-tagging discrimi-

nator has been determined from data, using $\mathrm{t\bar{t}}$ events for real b jets and Z+jets events for jets originating from light quarks. Data-to-simulation corrections have been obtained for these efficiencies and used to correct the number of b jets in the simulation, which translates into the number of events in the global `B-tag` and `No B-tag` event categories. In the eμ final state data-to-simulation corrections have been derived for the rate at which jets are misidentified as an electron or muon. These have been determined as a function of the jet p_{T} from Z+jets events in the $\mathrm{Z} \to \ell\ell$ decay. They are applied to W+jets and diboson events, which form more then 90% of the expected background due to jet $\to \ell$-misidentification in the eμ final state and where the flavor composition of jets is similar to that in the region in which the corrections have been determined. Corrections are further applied to $\mathrm{Z} \to \mu\mu$ events in the $\mu\tau_{\mathrm{h}}$ and $\tau_{\mathrm{h}}\tau_{\mathrm{h}}$ final states in which a muon is reconstructed as a τ_h candidate and in $\mathrm{Z} \to$ ee events in the $e\tau_h$ and $\tau_{\mathrm{h}}\tau_{\mathrm{h}}$ final states in which an electron is reconstructed as τ_h, to account for residual differences in the $\ell \to \tau_h$-misidentification rate between data and simulation. Finally a correction to the energy scale for electrons misidentified as τ_h is applied, which has been obtained from $\mathrm{Z} \to$ ee events. Corresponding uncertainties on all these corrections have been incorporated into the uncertainty model for the statistical inference of the signal as described in Section 6.

Deficiencies in the modeling of Drell-Yan events in the ee, $\mu\mu$ and $\tau\tau$ final states have been corrected for by a weighting of the simulated $\mathrm{Z} \to \mu\mu$ events to data in bins of $p_{\mathrm{T}}(\mu\mu)$ and $m(\mu\mu)$. The weights obtained have been applied to the simulated events in all leptonic final states. For the statistical inference of the signal the overall normalization of the background from $\mathrm{Z} \to \tau\tau$ events is furthermore constrained by dedicated control regions of $\mathrm{Z} \to \mu\mu$ events in each global event category, making use of lepton universality. Theoretical uncertainties arising from residual kinematic differences between the selected di-muon and di-τ final states have been incorporated into the uncertainty model. In addition all simulated $\mathrm{t\bar{t}}$ events have been weighted to better match the top quark p_{T} distribution as observed in data as described in Ref. [63]. For the statistical inference of the signal the overall normalization of this background is also constrained by a dedicated control region with an isolated electron, an isolated muon, and large E_T^{miss} in the final state; this sample has a $\mathrm{t\bar{t}}$ purity of 85%. All control regions used for the statistical inference of the signal are outlined in Fig. 3.

5.4 Cross checks of background estimations

Two cross checks are performed to give confidence in the background estimation. In a first cross check all backgrounds apart from QCD multijet production and the normalization for W+jets events are taken from simulation. For this purpose all corrections as summarized in Subsection 5.3 are applied to all simulated events. This cross check is performed in the eτ_{h} and $\mu\tau_{\mathrm{h}}$ final states.

The prediction of W+jets events, prior to the signal inference, is obtained by subtracting the small contribution of all other backgrounds except for QCD multijet and W+jets from data in corresponding control regions with $m_T^{e(\mu)} > 70\,\mathrm{GeV}$. An estimate for the normalization of the W+jets events can then be obtained from the following system of linear equations

$$\begin{aligned} N'^{SS}_{data} &= N^{SS}_{QCD} + N^{SS}_{\mathrm{W+jets}} \\ N'^{OS}_{data} &= f^{OS/SS}_{QCD} \cdot N^{SS}_{QCD} + f^{OS/SS}_{\mathrm{W+jets}} \cdot N^{SS}_{\mathrm{W+jets}}\,, \end{aligned} \tag{6}$$

where $N'^{SS(OS)}_{data}$ corresponds to the number of events in the control regions after subtracting the expected number of events for all other backgrounds and $f^{OS/SS}_{QCD(\mathrm{W+jets})}$ is the expected opposite-

sign to same-sign ratio for W+jets and QCD multijet events. For this estimate $f^{OS/SS}_{\text{W+jets}}$ has been obtained from the simulation and $f^{OS/SS}_{QCD}$ from another control region with inverted isolation requirements on the electron or muon, as described below. An estimate for $N^{SS}_{\text{W+jets}}$ can then be obtained from Eq. (6). From this the number of W+jets events in the SR can be inferred via $f^{OS/SS}_{\text{W+jets}}$ and another extrapolation factor from the control region into the SR, which again has been taken from the simulation. To stay as close as possible to the kinematic regime in the signal regions an opposite-sign and a same-sign control region for the determination of N'^{OS}_{data} and N'^{SS}_{data} have been defined, for each event sub-category in the $e\tau_h$ and $\mu\tau_h$ final states, as described in Section 4, which amounts to eight control regions per final state. The shape of the final discriminating variable used for the statistical inference of the signal is taken from simulation.

The shape and normalization prior to the statistical inference of the signal for QCD multijet events are obtained from control regions equivalent to the signal regions with the exception of a same-sign instead of an opposite-sign requirement on the charge of the selected di-τ pair. From the events in this control region all other expected backgrounds are subtracted using the normalization and shape information for the final discriminating variable from simulation with the exception of the normalization of W+jets events, which is obtained as described above. The extrapolation factors ($f^{OS/SS}_{QCD}$) from same-sign to opposite-sign are obtained from control regions, where in addition to the opposite-sign or same-sign requirement the isolation requirement on the electron or muon has been inverted. The extrapolation factors are then obtained from a fit to the data in the control regions similar to the one used for the statistical inference of the signal described in Section 6. To control the normalization of the W+jets and QCD multijet events the eight additional control regions per final state, as introduced above, are added to the fit for the statistical inference of the signal and the corresponding normalization uncertainties are incorporated into a modified uncertainty model. This corresponds to an extension of the background model that has been used in earlier versions of this analysis.

In a second cross check the background from $Z \to \tau\tau$ events in the main analysis is replaced with the prediction obtained from the $\mu \to \tau$ embedding method as used during the LHC Run 1 analyses and described, for example, in Refs. [64, 65]. In this process $Z \to \mu\mu$ events are selected in data. The muons are then replaced by simulated τ decays with the same kinematics as the reconstructed muons. In this way the method relies only on the simulation of the well understood τ decay while all other parts of the event are obtained from data. As a consequence several data-to-simulation corrections as described in Subsection 5.3, which are of particular importance for the event categorization as well as for the shape of the final discriminating variable cancel out for this process. This applies, for example, to corrections of the jet energy scale, b-tagging efficiency and $\vec{p}^{\,\text{miss}}_T$. This cross check is applied in the $e\tau_h$, $\mu\tau_h$, and $\tau_h\tau_h$ final states individually. Both the extrapolation factors from the inclusive event selection into the event sub-categories as well as the shapes of the final discriminating variable for the statistical inference of the signal, obtained from the simulation, are found to be in good agreement with the estimates as obtained from the embedding method, within the estimated uncertainties. In addition the uncertainties that are related to the experimental aspects of the $\mu \to \tau$ embedding, which are orthogonal to the uncertainties in the estimate from simulation, are incorporated into a modified uncertainty model to replace several uncertainties for the estimate based on the simulation.

6 Statistical inference for the signal

The final discriminating variable used to search for a signal is the total transverse mass, $m_{\mathrm{T}}^{\mathrm{tot}}$ [26], defined as

$$m_{\mathrm{T}}^{\mathrm{tot}} = \sqrt{m_{\mathrm{T}}^2(E_{\mathrm{T}}^{\mathrm{miss}}, \tau_1^{\mathrm{vis}}) + m_{\mathrm{T}}^2(E_{\mathrm{T}}^{\mathrm{miss}}, \tau_2^{\mathrm{vis}}) + m_{\mathrm{T}}^2(\tau_1^{\mathrm{vis}}, \tau_2^{\mathrm{vis}})}\,, \tag{7}$$

where the index in τ_i^{vis} corresponds to the final state label and the transverse mass between two objects is given by

$$m_{\mathrm{T}}(1,2) = \sqrt{2 p_{\mathrm{T}}(1) p_{\mathrm{T}}(2)(1 - \cos\Delta\phi(1,2))}, \tag{8}$$

so that $m_{\mathrm{T}}(E_{\mathrm{T}}^{\mathrm{miss}}, \tau_1^{\mathrm{vis}})$ is equivalent to the transverse mass as defined for the $\mathrm{e}\tau_{\mathrm{h}}$ and $\mu\tau_{\mathrm{h}}$ final states in Eq. (3). The input distributions to the statistical inference of the signal in a subset of the most sensitive event sub-categories per final state are shown in Figs. 5 and 6. The expected $m_{\mathrm{T}}^{\mathrm{tot}}$ distribution is represented by the stack of filled histograms in the upper panel of each sub-figure, where each filled histogram corresponds to the estimated template distribution of the SM process that has been taken into account for the analysis. For this purpose the contributions from QCD multijet, W+jets and $\mathrm{t\bar{t}}$ events contributing to the event selection by jet $\to \tau_h$-misidentification are subsumed into one single contribution labeled as "jet $\to \tau_h$ fakes". The remaining contributions from W+jets, single top quark and diboson events are subsumed into one single contribution labeled as "Electroweak". The shaded band associated with the sum of filled histograms corresponds to the combined uncertainty in all background processes, taking into account all correlations as obtained from the fit used for the statistical inference of the signal. In the lower panel of each sub-figure the ratio of the data points to the expectation from the sum of all filled histograms is shown; the statistical uncertainty in the data is represented by error bars and the uncertainty in all background processes by the shaded band. The expected $m_{\mathrm{T}}^{\mathrm{tot}}$ distribution for a signal of three neutral Higgs bosons from gluon-fusion and b-associated production in the MSSM $m_h^{\mathrm{mod+}}$ [16] scenario for $m_A = 700\,\mathrm{GeV}$ and $\tan\beta = 20$ is also shown.

For the statistical inference of the signal a simultaneous binned maximum likelihood fit to the $m_{\mathrm{T}}^{\mathrm{tot}}$ distributions in all event sub-categories and all final states is performed. This is done under the background-only and several signal-plus-background hypotheses to search for potential excesses due to the presence of additional Higgs bosons over the known SM processes. For this purpose the SM Higgs boson is included in the background processes. The control regions, which have been designed to constrain the background from Drell-Yan and $\mathrm{t\bar{t}}$ events, are included in the likelihood model, resulting in a fit in sixteen event sub-categories and three control regions as outlined in Fig. 3.

The data are interpreted in two ways based on the ratio of the fitted likelihoods for the background-only and the tested signal-plus-background hypothesis. For each interpretation the model for the background processes is formed from the template distributions as shown, for example, in Figs. 5 and 6. In the first interpretation, which is meant to be as model-independent as possible, the signal model corresponds to a single resonance in addition to the expected SM processes assuming the narrow width approximation. For this purpose 28 simulated single resonances for a neutral Higgs boson between 90 GeV and 3.2 TeV in the gluon-fusion and b-associated production modes have been used. The signal is searched for in both production modes at the same time using two freely varying parameters of interest for the statistical inference, one for each production mode. In the second interpretation the simulated mass points

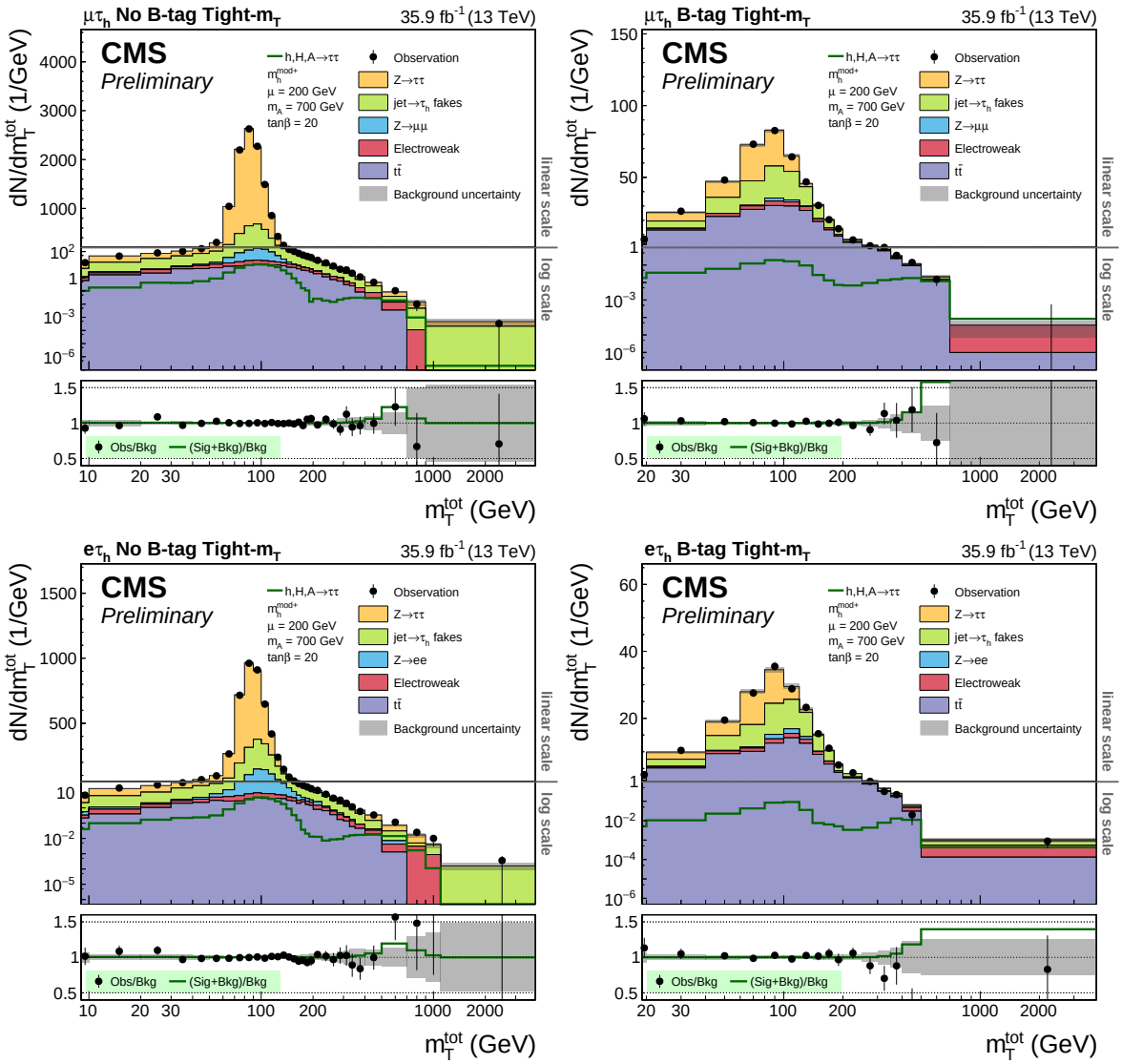

Figure 5: Distribution of $m_{\mathrm{T}}^{\mathrm{tot}}$ in the global (left) `No B-tag` and (right) `B-tag` categories in the (upper row) $\mu\tau_{\mathrm{h}}$ and (lower row) $\mathrm{e}\tau_{\mathrm{h}}$ final states. In all cases the most sensitive `Tight-`m_T event sub-category is shown. The black horizontal line indicates the change from logarithmic to linear scale on the vertical axis.

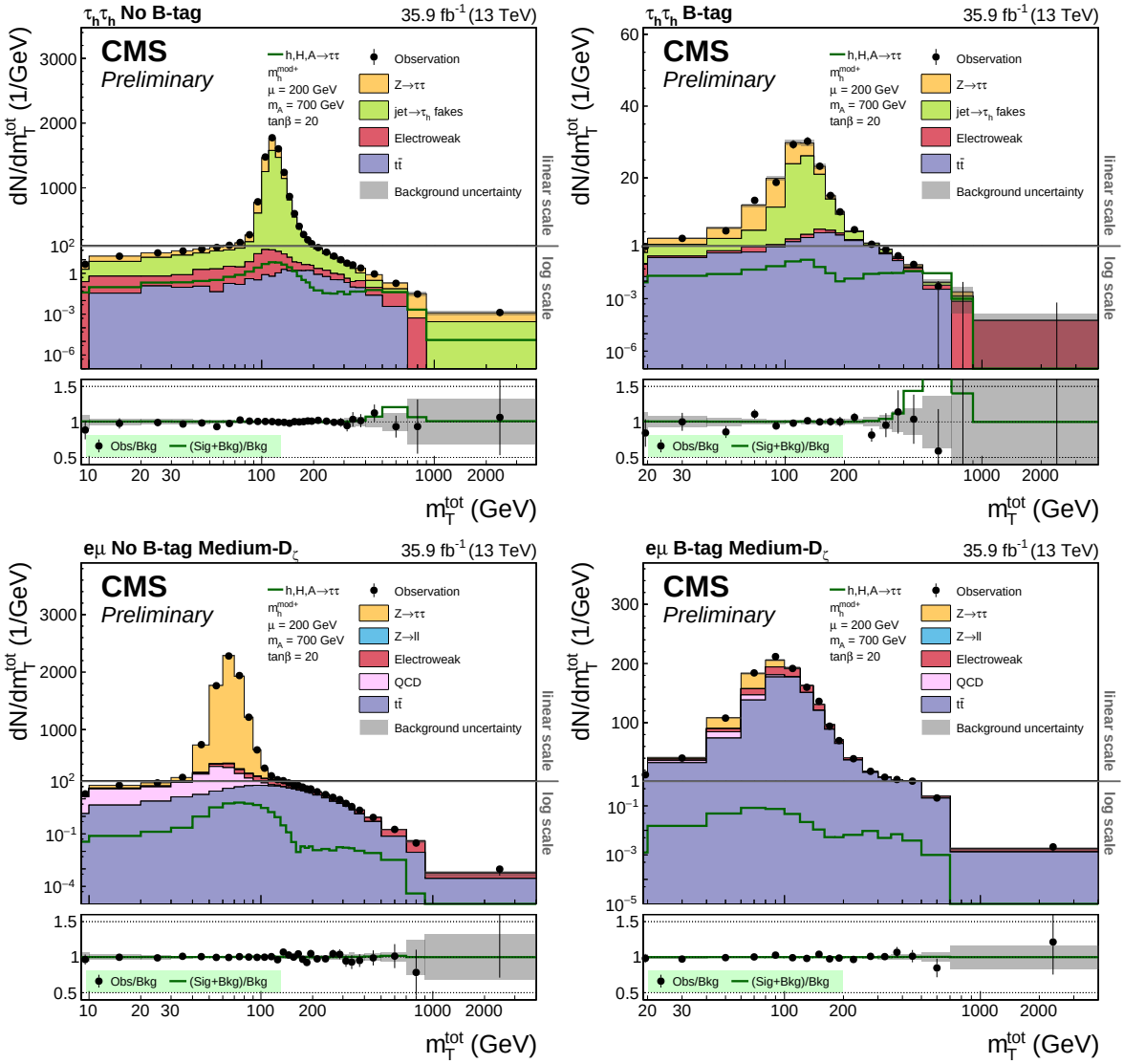

Figure 6: Distribution of $m_{\mathrm{T}}^{\mathrm{tot}}$ in the global (left) `No B-tag` and (right) `B-tag` categories in the (upper row) $\tau_{\mathrm{h}}\tau_{\mathrm{h}}$ and (lower row) eμ final states. For the eμ final state the most sensitive `Medium-`D_ζ event sub-category is shown. The black horizontal line indicates the change from logarithmic to linear scale on the vertical axis.

are combined into the multi-resonance signal structure expected from each of the tested MSSM benchmark scenarios. This is done using the model predictions as described in Subsection 5.1 and a linear template morphing algorithm as described in Ref. [66] to move the simulated mass points to their exact predicted values.

The uncertainty model comprises theoretical uncertainties, experimental uncertainties, and uncertainties due to the limited population of the template distributions used for the prediction of the background processes. The latter are most important for the high-mass searches. All systematic uncertainties are implemented in the form of nuisance parameters in the likelihood, which can be further constrained by the fit to the data. The following uncertainties have been implemented as normalization uncertainties that leave the shape of the $m_{\mathrm{T}}^{\mathrm{tot}}$ distributions unchanged:

- The uncertainty in the integrated luminosity measurement has been found to be 2.5% [67]. This uncertainty is applied to all processes that have been estimated from simulation.
- The uncertainties in the measurement of the identification, isolation and trigger efficiencies have been found to amount to 2% both for electrons and muons, adding all individual contributions in quadrature. These uncertainties are applied to all processes that have been estimated from simulation.
- Uncertainties in the measurement of the probability of electrons ($\mathrm{e} \to \tau_{\mathrm{h}}$) and muons ($\mu \to \tau_{\mathrm{h}}$) to be misidentified as τ_h are applied to the fraction of simulated Drell-Yan events with light leptons being misidentified as τ_h in the $\mathrm{e}\tau_{\mathrm{h}}$, $\mu\tau_{\mathrm{h}}$ and $\tau_{\mathrm{h}}\tau_{\mathrm{h}}$ final states. The uncertainty in the $\mathrm{e} \to \tau_{\mathrm{h}}$ misidentification probability amounts to 11% (3%) in the $\mathrm{e}\tau_{\mathrm{h}}$ ($\tau_{\mathrm{h}}\tau_{\mathrm{h}}$) final state. The uncertainty in the $\mu \to \tau_{\mathrm{h}}$ misidentification probability is 12% (5%) in the $\mu\tau_{\mathrm{h}}$ ($\tau_{\mathrm{h}}\tau_{\mathrm{h}}$) final state.
- The uncertainty in the τ_h-identification efficiency has been found to be 5%. It is factorized into a 4% (8%) part that is correlated and a 3% (9.2%) part that is uncorrelated across the $\mathrm{e}\tau_{\mathrm{h}}$ and $\mu\tau_{\mathrm{h}}$ ($\tau_{\mathrm{h}}\tau_{\mathrm{h}}$) final states. The uncorrelated part contains a 7% uncertainty in the τ_h trigger efficiency measurement in the $\tau_{\mathrm{h}}\tau_{\mathrm{h}}$ final state. The τ_h related uncertainties are applied to all processes that have been estimated from simulation and that contain genuine hadronic tau leptons.
- The uncertainty in the jet energy scale affects the number of events entering each category. It is applied to all processes estimated from simulation and ranges from 1–6%, depending on the final state and sub-category. Similarly, uncertainties in the rate with which both light jets and genuine b jets pass the b-tagging discriminator are applied to all processes estimated from simulation. These uncertainties range from 1–5% in size.
- Uncertainties in the resolution and response of the $E_{\mathrm{T}}^{\mathrm{miss}}$ are derived as part of the determination of the recoil corrections. This leads to uncertainties of between 1–5% that are incorporated for all processes estimated from simulation and to which recoil corrections have been applied. These are all signal processes, Drell-Yan production and W+jets events. For the single top quark, diboson and $\mathrm{t\bar{t}}$ backgrounds, which do not have recoil corrections applied, jet energy scale and unclustered energy scale variations are propagated to the $E_{\mathrm{T}}^{\mathrm{miss}}$, also leading to uncertainties ranging from 1–5%.
- The theoretical uncertainty in the cross section calculations for the single top quark and diboson contribution amounts to 5%. In the $\mathrm{e}\mu$ final state, where the W+jets contribution is taken from simulation, the theoretical uncertainty in the cross section

calculation is 4%. Due to the inclusion of the $Z \to \mu\mu$ control regions and the $t\bar{t}$ control region in the model for the statistical inference of the signal, which control the Drell-Yan and $t\bar{t}$ normalization respectively, no theoretical cross section uncertainties are applied for these processes. However, uncertainties are applied to the $Z \to \tau\tau$, $Z \to \ell\ell$ and $t\bar{t}$ processes in all signal categories to account for the extrapolation from the control region to the signal region. The $Z \to \tau\tau$ extrapolation uncertainties range from 1–7%. The extrapolation uncertainties for $Z \to \ell\ell$ events are 4%. The extrapolation uncertainties from the $t\bar{t}$ control region to the signal regions are found to be below 1%. An additional uncertainty of 1% is however applied in the $t\bar{t}$ control region to account for fluctuations in the variables used to select the events in this control region. The uncertainty in the estimation of the backgrounds in the DR_i for the determination of the fake factors is applied to the background contributions estimated from the fake factor method. This uncertainty amounts to 3% (4%) in the $e\tau_h$ and $\mu\tau_h$ ($\tau_h\tau_h$) final states.

- Since the background from QCD multijet events in the $e\mu$ final state is determined from a control region, uncertainties that account for the statistical uncertainty in the data and the subtracted backgrounds in this control region are applied. In addition, this background is subject to uncertainties related to the extrapolation from the control region to the signal regions. An overall 30% extrapolation uncertainty is applied, in addition to category-dependent uncertainties ranging from 4–29%, in the measurement of the opposite-sign to same-sign correction.
- Theoretical uncertainties on the b-associated signal acceptance are obtained from variations of the renormalization (μ_r) and factorization (μ_f) scales and of the generator-internal matching scale Q_{sh} related to parton showering. The scales μ_r and μ_f are varied by factors of 0.5 and 2. The scale uncertainty is obtained from the envelope of the six variations of μ_r and μ_f, as recommended in Ref. [68]. Depending on the tested mass it ranges between -4% (for 90 GeV), -0.4% (for 500 GeV) and -2.5% (for 3.2 TeV) in the `B-tag` categories and 0.8% (for 90 GeV), 0.3% (for 500 GeV) and 2.0% (for 3.2 TeV) in the `No B-tag` categories. The scale Q_{sh} is varied by factors of $1/\sqrt{2}$ and $\sqrt{2}$. The resulting uncertainty ranges between -13.2% (for 90 GeV), -4.6% (for 500 GeV) and -1.8% (for 3.2 TeV) in the `B-tag` categories and 2.6% (for 90 GeV), 2.9% (for 500 GeV) and 1.4% (for 3.2 TeV) in the `No B-tag` categories. The uncertainty from the variation of μ_r and μ_f and the uncertainty from the variation of Q_{sh} are added linearly, following the recommendation in Ref. [68].
- For the parameter scan in the model interpretations, theoretical uncertainties due to the different choices of the factorization and renormalization scales on the signal predictions are included. The MSTW2008 [69] parton distribution functions are used for the calculation of the production cross sections. The uncertainties on the choice for the parton distribution functions are calculated following the recommended prescription given in Refs. [69, 70]. The uncertainties are evaluated separately for each m_A-tan β point. They vary between 15% and 25%.
- For all results shown in the following the SM Higgs boson is taken into account in the likelihood ratio. Uncertainties due to different choices of the renormalization and factorization scales for the calculation of the production cross section of the SM Higgs boson amount to 3.9% for gluon-fusion, 0.4% for VBF, 2.8% for Z-associated and 0.5% for W-associated production. Uncertainties due to different choices for the parton density functions and α_s amount to 3.2% for gluon-fusion, 2.1% for VBF, 1.6% for Z-associated and 1.9% for W-associated production. The procedure for deriving

these uncertainties is further described in Ref. [68].

The following systematic uncertainties allow correlated changes across bins in the $m_{\mathrm{T}}^{\mathrm{tot}}$ input distributions, i.e. they alter the shape of the distributions, and are referred to as shape uncertainties hereafter:

- Three independent uncertainties are applied on the energy scale for genuine τ_h decays; for the decay into a single charged hadron with and without neutral pions and the decay into three charged hadrons. Each uncertainty is 1.2%. They affect both the normalization and the shape of $m_{\mathrm{T}}^{\mathrm{tot}}$ for the signal, the $\mathrm{Z} \to \tau\tau$, $\mathrm{t\bar{t}}$ and diboson backgrounds containing genuine tau leptons in the $\mathrm{e}\tau_{\mathrm{h}}$, $\mu\tau_{\mathrm{h}}$ and $\tau_{\mathrm{h}}\tau_{\mathrm{h}}$ final states.
- An uncertainty of $+5\% \times p_{\mathrm{T}}[\mathrm{TeV}]$ and $-35\% \times p_{\mathrm{T}}[\mathrm{TeV}]$ is applied to account for the extrapolation in the τ_h-identification efficiency estimate, which is mostly determined by low p_{T} τ_h decays close to the Z peak, to higher p_{T} regimes of the tau leptons that are particularly relevant for the high mass signal hypotheses. This uncertainty is applied to the signal, the $\mathrm{Z} \to \tau\tau$, $\mathrm{t\bar{t}}$ and diboson backgrounds containing genuine tau leptons in the $\mathrm{e}\tau_{\mathrm{h}}$, $\mu\tau_{\mathrm{h}}$ and $\tau_{\mathrm{h}}\tau_{\mathrm{h}}$ final states.
- In the $\mathrm{e}\tau_{\mathrm{h}}$ final state, an uncertainty in the energy scale of electrons misidentified as τ_h is applied, split into a 1% (0.5%) absolute uncertainty in the correction for the decay mode with one charged hadron with (without) neutral pions. This uncertainty is only applied to the $\mathrm{Z} \to \mathrm{ee}$ process where one of the electrons is misidentified as a τ_h.
- In the $\mathrm{e}\mu$ final state, an uncertainty in the electron energy scale is applied that amounts to 1% in the barrel and 2.5% in the endcaps.
- An uncertainty in the correction of the momentum of the top quarks in simulated $\mathrm{t\bar{t}}$ events is applied that corresponds to 100% of the correction as discussed in Subsection 5.3. This affects this background in all signal regions and in the $\mathrm{t\bar{t}}$ control region. This uncertainty is further constrained by the $\mathrm{t\bar{t}}$ control region described in Section 4.
- Five uncertainties are included to cover the uncertainty in the reweighting method to improve the modeling of the simulation of Drell-Yan events as described in Subsection 5.3. These uncertainties include the propagation of the 0.2% muon energy scale uncertainty to the derived weights and the propagation of a 6% $\mathrm{t\bar{t}}$ cross section uncertainty, which affects the simulated $\mathrm{t\bar{t}}$ background that needs to be subtracted in the $\mathrm{Z} \to \mu\mu$ selection. Since the reweighting is obtained prior to the statistical inference for the signal this is not coupled to the $\mathrm{t\bar{t}}$ control region. In addition, the statistical uncertainties on the measured weights were found to be non-negligible in three of the bins used to derive the correction, which leads to three additional shape uncertainties related to the reweighting procedure.
- In the $\mathrm{e}\mu$ final state, shape uncertainties are applied to all processes with jets misidentified as muons or electrons to account for the uncertainties in the jet$\to$ e and jet$\to$ μ misidentification probability. The size of these uncertainties depends on the jet p_{T}, with a minimum uncertainty of 13% (10%) for electrons (muons).

In the $\mu\tau_{\mathrm{h}}$, $\mathrm{e}\tau_{\mathrm{h}}$ and $\tau_{\mathrm{h}}\tau_{\mathrm{h}}$ final state the following shape uncertainties related to the fake factor method are applied to those background components that have been estimated by this method:

- Statistical uncertainties in the estimate of the FF_i in the DR_i are obtained from the uncertainties of the fit used to parametrize the FF_i. They amount to 4% in $\mu\tau_{\mathrm{h}}$ final state and range between 4–7% (2–3%) ind $\mathrm{e}\tau_{\mathrm{h}}$ ($\tau_{\mathrm{h}}\tau_{\mathrm{h}}$) final state.

- In the $e\tau_h$ and $\mu\tau_h$ final states uncertainties are taken into account in the corrections due to the finite number of events or omitted dependencies during the fake factor determination. This is done for all backgrounds considered. Additional uncertainties are taken into account on all background specific corrections that are applied to the FF_i. For FF_{QCD} these are the correction of the extrapolation from the same-sign to the opposite-sign region and the correction as a function of the lepton isolation. For FF_{W+jets} this is the correction as a function of the transverse mass. For $FF_{t\bar{t}}$ this is the data-to-simulation correction in the dedicated control region. All these uncertainties are added in quadrature for each corresponding background and vary between 7–10% in the $e\tau_h$ and 5–7% in the $\mu\tau_h$ final states.
- In the $\tau_h\tau_h$ final state uncertainties are taken into account in the corrections due to the finite number of events or omitted dependencies during the fake factor determination. Additional uncertainties in the correction of the same-sign to opposite-sign extrapolation as a function of the p_T of the other τ_h candidate, in the estimate of the fractions of W+jets, Drell-Yan and $t\bar{t}$ events with one jet misidentified as τ_h and in the use of FF_{QCD} for the estimation of the W+jets and $t\bar{t}$ contributions to the total jet $\rightarrow \tau_h$ background are taken into account. When added in quadrature, these additional uncertainties are of the order of 10%.

The shape uncertainties related to the fake factor method are factorized into a pure shape and pure normalization part. The normalization terms of the statistical uncertainties are added in quadrature for each individual category in each final state and applied as normalization uncertainties. In addition uncertainties due to the limited population of the template distributions used for the prediction of the background processes are taken into account by allowing each bin of each background template to vary within its statistical uncertainty. These uncertainties are uncorrelated across the bins of the input distributions.

An overview of all uncertainties that have been taken into account in the likelihood model for the statistical inference of the signal is given in Table 3.

7 Results

The complete model used for the statistical inference of the signal results in a likelihood function of the form

$$\mathcal{L}\left(\{k_i\}|\,\mu s(\theta)+b(\theta)\right) = \prod_i \mathcal{P}(k_i|\mu s_i(\theta)+b_i(\theta)) \times \prod_j \mathcal{C}(\hat{\theta}_j|\theta_j)\,, \tag{9}$$

where i labels all bins of the input distributions in all event sub-categories and control regions and j all nuisance parameters. The term θ_j corresponds to a given nuisance parameter, μ to a scaling parameter for a given signal s_i and b_i to the prediction of all backgrounds in bin i. The function $\mathcal{P}(k_i|\mu s_i(\theta)+b_i(\theta))$ corresponds to a Poisson distribution, $\mathcal{C}(\hat{\theta}_j|\theta_j)$ to the probability density function used to implement the uncertainty related to the nuisance parameter θ_j and $\hat{\theta}_j$ to the estimate for θ_j from the fit to the data. All distributions shown in Figs. 5 and 6 are after an MSSM m_h^{mod+} signal-plus-background hypothesis, corresponding to $m_A = 700\,\text{GeV}$ and $\tan\beta = 20$, has been fitted to the data.

No signal is observed in the investigated mass range between 90 GeV and 3.2 TeV. For this reason upper limits on the presence of a signal are set in the two interpretations of the data as discussed in Section 6. This is done following the modified frequentist approach as described

in Refs. [71, 72], using the same definition of the test statistic as in the search for the SM Higgs boson [73, 74]:

$$q_\mu = -2\ln\left(\frac{\mathcal{L}(\{k_i\}|\,\mu s(\hat{\theta}_\mu) + b(\hat{\theta}_\mu))}{\mathcal{L}(\{k_i\}|\,\hat{\mu} s(\hat{\theta}_{\hat{\mu}}) + b(\hat{\theta}_{\hat{\mu}}))}\right), \quad 0 \leq \hat{\mu} \leq \mu, \tag{10}$$

where the hat again indicates the estimate from the fit to the data and the index of q_μ indicates that the fit to the data has been performed for a fixed parameter μ. In the large number limit the distribution of q_μ can be approximated by analytic functions, from which the median and the uncertainty contours can be obtained.

In the first interpretation of the data 95% confidence level (CL) upper limits are set on the product of the cross section and branching fraction into a di-τ pair for the gluon-fusion and b-associated production of a single resonance, under the narrow width approximation. In Fig. 7 these limits are shown as a function of the tested Higgs boson mass. For the determination of the limit on one process, e.g. gluon-fusion, the normalization for the corresponding other process, e.g. b-associated production, has been treated as a freely varying parameter in the signal-plus-background fit that is performed prior to the limit calculation. The expectation for a SM Higgs boson at 125 GeV has been taken into account in the SM backgrounds. For both production modes the p_T spectrum of the Higgs boson is estimated at NLO precision in α_s, as described in Subsection 5.1. Differences in the sensitivity of the analysis only occur at low masses, where the p_T of the Higgs boson significantly contributes to the p_T of its decay products. In the figure this is emphasized by adding the median for the expected limit using either only the b quark or only the t quark for the modeling of the Higgs boson p_T spectrum. For the production via gluon-fusion the expected limits range between $\approx$18 pb (at 90 GeV) and $\approx 3.5 \times 10^{-3}$ pb (at 3.2 TeV). For b-associated production they range between $\approx$15 pb (at 90 GeV) and 2.5×10^{-3} pb (at 3.2 TeV). In both cases, the excluded cross section falls with increasing mass, before becoming constant at around 1 TeV. No significant deviation from the expectation is observed. When restricted to the $e\tau_\mathrm{h}$, $\mu\tau_\mathrm{h}$ or $\tau_\mathrm{h}\tau_\mathrm{h}$ final state the results obtained from the cross checks summarized in Subsection 5.4 are compatible with the results obtained from the main analysis described in this paper. A three dimensional scan of the likelihood for this signal model is also performed, as a function of the gluon-fusion and b-associated production cross section and the tested mass points. A representative subset of this likelihood scan at six mass points is shown in Fig. 8.

In the second interpretation of the data exclusion contours in the m_A-tan β plane are determined for two representative benchmark scenarios of the MSSM, the $m_\mathrm{h}^{\mathrm{mod+}}$ [16] and the hMSSM [75–77] scenario. The $m_\mathrm{h}^{\mathrm{mod+}}$ scenario is compatible with the observation of the Higgs boson at 125 GeV; the boson at 125 GeV is interpreted as the h within the theoretical uncertainties in m_h of $\pm$3 GeV [78, 79]. The phenomenological hMSSM also incorporates the observed Higgs boson at 125 GeV, again interpreting it as the h boson. The uncertainties on the mass measurement are then used in turn to estimate the main radiative corrections to predict the masses and couplings of the remaining MSSM Higgs bosons.

For the determination of the exclusion contours the model predictions as provided by the LHC Higgs Cross Section Working Group [68, 80] are used. Inclusive cross sections for the production via gluon-fusion were calculated using the program SusHi [81] (v1.4.1). NLO QCD corrections in the context of the MSSM [82–87] are included in these calculations, as well as NNLO QCD corrections for the top quark contribution to the gluon-fusion loop in the heavy top quark limit [88–92], and electroweak effects from light quarks [93, 94]. For b-associated pro-

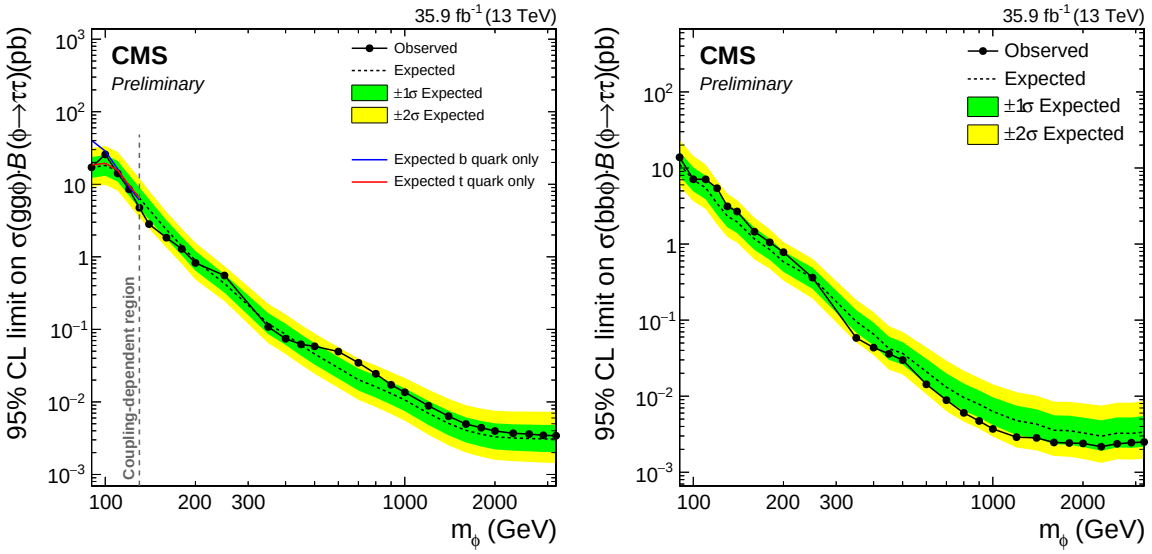

Figure 7: Expected and observed 95% CL upper limits for the production of a single narrow resonance ϕ with a mass between 90 GeV and 3.2 TeV in the di-τ final state (left) for the production via gluon-fusion and (right) in association with b quarks. The expected median of the exclusion limit is shown by the dashed line. The dark green and bright yellow band indicate the 68% and 95% confidence intervals for the variation of the expected exclusion limit. The black dots correspond to the observed limits.

duction four-flavor scheme NLO QCD calculations [95, 96] and five-flavor scheme NNLO QCD calculations, as implemented in SUSHI based on BBH@NNLO [97], have been combined using the Santander matching scheme [98]. The Higgs boson masses and mixing, and the effective Yukawa couplings for the $m_h^{\text{mod+}}$ scenario, have been calculated using the FEYNHIGGS [78, 99–102] (v2.10.2) code. The branching fraction of the Higgs boson to tau leptons was calculated with FEYNHIGGS for the $m_h^{\text{mod+}}$ scenario and using the program HDECAY [103] (v6.40) for the hMSSM scenario.

The simulated single neutral Higgs boson signals are combined into a multi-resonance signal model for the given values of m_{A} and $\tan\beta$, taking into account the predictions for the mass, production cross sections and branching fraction into tau leptons for each of the neutral Higgs bosons. For each value of m_{A} and $\tan\beta$, using a fine grain scan, a maximum likelihood fit to the data is performed under the background-only and the signal-plus-background hypotheses using the likelihood of Eq. (9) but with a modified test statistic as given in Eq. (10). The numerator remains the same, with a fixed value of $\mu = 1$, and corresponds to the signal prediction for the given value in m_{A} and $\tan\beta$. However no signal strength parameter is included in the denominator; the model is thus fixed to the background-only prediction and the SM Higgs boson is added to the non-Higgs boson background processes. This turns the likelihood ratio into a comparison between the MSSM and the SM Higgs sector hypotheses, and ensures a well defined problem even when reaching the sensitivity for the observed Higgs boson at 125 GeV. The median and confidence intervals for the expected exclusion contour are determined from toys. In Fig. 9 the observed and expected exclusion contours for the MSSM $m_{\text{h}}^{\text{mod+}}$ and the hMSSM scenarios are shown. In both scenarios the exclusion contours extend down to values of $\tan\beta \approx 6$ for values of $m_{\text{A}} \lesssim 250$ GeV. Thus from the analyzed dataset a heavy MSSM Higgs boson within this mass range is practically excluded in both scenarios. The exclusion contours reach up to 1.6 TeV, extending the excluded mass range by almost a factor of two in m_{A} com-

pared to the previous CMS publication using this final state. Over the whole mass range the observed exclusion contours follow the expectation with the largest deviations still contained in the 95% confidence interval.

8 Summary

A search for additional heavy neutral Higgs bosons in the decay into two tau leptons in the context of the MSSM has been presented. This search has been performed in the most sensitive $e\mu$, $e\tau_h$, $\mu\tau_h$ and $\tau_h\tau_h$ final states of the di-τ pair, where τ_h indicates a hadronic τ decay. The sensitivity of the analysis has been increased by splitting the resulting events into sixteen signal categories. These have been complemented by three control regions to constrain the normalization of the backgrounds from Drell-Yan and $t\bar{t}$ events in situ during the fits to the data that are performed for the statistical inference of the signal. The signal categorization is motivated by the expected enhancement of the coupling of the heavy neutral Higgs bosons to *down*-type fermions for the most interesting MSSM parameter space, corresponding to values of $\tan\beta > 1$. This enhancement influences the kinematics of the production via gluon-fusion and leads to an increased cross section for b-associated production. A signal has been searched for in a combined maximum likelihood fit to all signal categories and control regions in all final states under investigation. No signal has been found. Model-independent limits have been set for the production of a single narrow resonance. These range from 18 pb (at 90 GeV) to 3.5×10^{-3} pb (at 3.2 TeV) for the production via gluon-fusion and from 15 pb (at 90 GeV) to 2.5×10^{-3} pb (at 3.2 TeV) for b-associated production. These limits are supplemented by a three dimensional likelihood scan as a function of the product of the production cross section and di-τ branching fraction for gluon-fusion, b-associated production and the tested mass. Finally exclusion contours have been provided for two representative benchmark scenarios namely the $m_h^{\text{mod+}}$ and the hMSSM scenarios. In these two scenarios the presence of a neutral heavy MSSM Higgs boson up to $m_A \lesssim 250$ GeV is excluded for $\tan\beta$ values above 6. The exclusion contour ranges up to 1.6 TeV for $\tan\beta < 60$.

Table 3: Overview of the systematic uncertainties used in the likelihood model for the statistical inference of the signal. The expression "sim." refers to all processes that have been obtained from simulation, the expression "FF" refers to all backgrounds that are obtained from the fake factor method. Values in brackets correspond to additional uncertainties correlated across final states or event categories. Detailed descriptions are given in the text.

uncertainty	$e\mu$	$e\tau_h$	$\mu\tau_h$	$\tau_h\tau_h$	process	shape	variation
luminosity	✓	✓	✓	✓	sim.	–	2.5%
e/μ-trigger, ID, isolation	✓	✓	–	–	sim.	–	2%
		–	✓				2%
jet → e mis-ID	✓	–	–	–	sim.	✓	13%
jet → μ mis-ID	✓	–	–	–	sim.	✓	10%
e → τ_h mis-ID	–	✓	–	–	Z → ee	–	11%
		–		✓			3%
μ → τ_h mis-ID	–	–	✓	–	Z → $\mu\mu$	–	12%
			–	✓			5%
τ_h-trigger	–	–	–	✓	sim.	–	7%
τ_h-ID	–	✓	✓	–	sim.	–	3%(4%)
		–	–	✓			6%(8%)
τ_h-ID (high p_T)	–	✓	✓	✓	sim.	✓	p_T dep.
τ_h energy scale	–	✓	✓	✓	sim.	✓	1.2%
e → τ_h energy scale	–	✓	–	–	Z → ee	✓	0.5–1%
e energy scale	✓	–	–	–	sim.	✓	1–2.5%
jet energy scale	✓	✓	✓	✓	sim.	–	1–6%
b-tagging	✓	✓	✓	✓	sim.	–	1–5%
E_T^{miss} resp./res.	✓	✓	✓	✓	sim.	–	1–5%
sideband extrap.	✓	✓	✓	✓	Z → $\tau\tau$	–	1–7%
	✓	✓	✓	✓	Z → $\ell\ell$		4%
	✓	✓	✓	✓	$t\bar{t}$		1%
	✓	–	–	–	QCD		4–29% (30%)
bkgr. in signal categories	✓	✓	✓	✓	diboson	–	5%
		✓	✓	✓	single top		5%
		–	–	–	W+jets		4%
bkgr. in $DR_{QCD/W+jets}$	–	✓	✓	–	sim.	–	3%
		–	–	✓			4%
FF_i stat. uncert.	–	✓	–	–	FF	✓	4–7%
		–	✓	–			4%
		–	–	✓			2–3%
FF_i corrections	–	✓	–	–	FF	✓	7–10%
		–	✓	–			5–7%
		–	–	✓			10%
top quark p_T reweighting	✓	✓	✓	✓	$t\bar{t}$	✓	100%
Z reweighting of LO sim.	✓	✓	✓	✓	Z → $\tau\tau, \ell\ell$	✓	see text
b-associated signal acc.	✓	✓	✓	✓	signal	–	3.2–16.5%
signal pdf/scale	✓	✓	✓	✓	signal	–	15–20%
					SM Higgs		0.5–3.2%

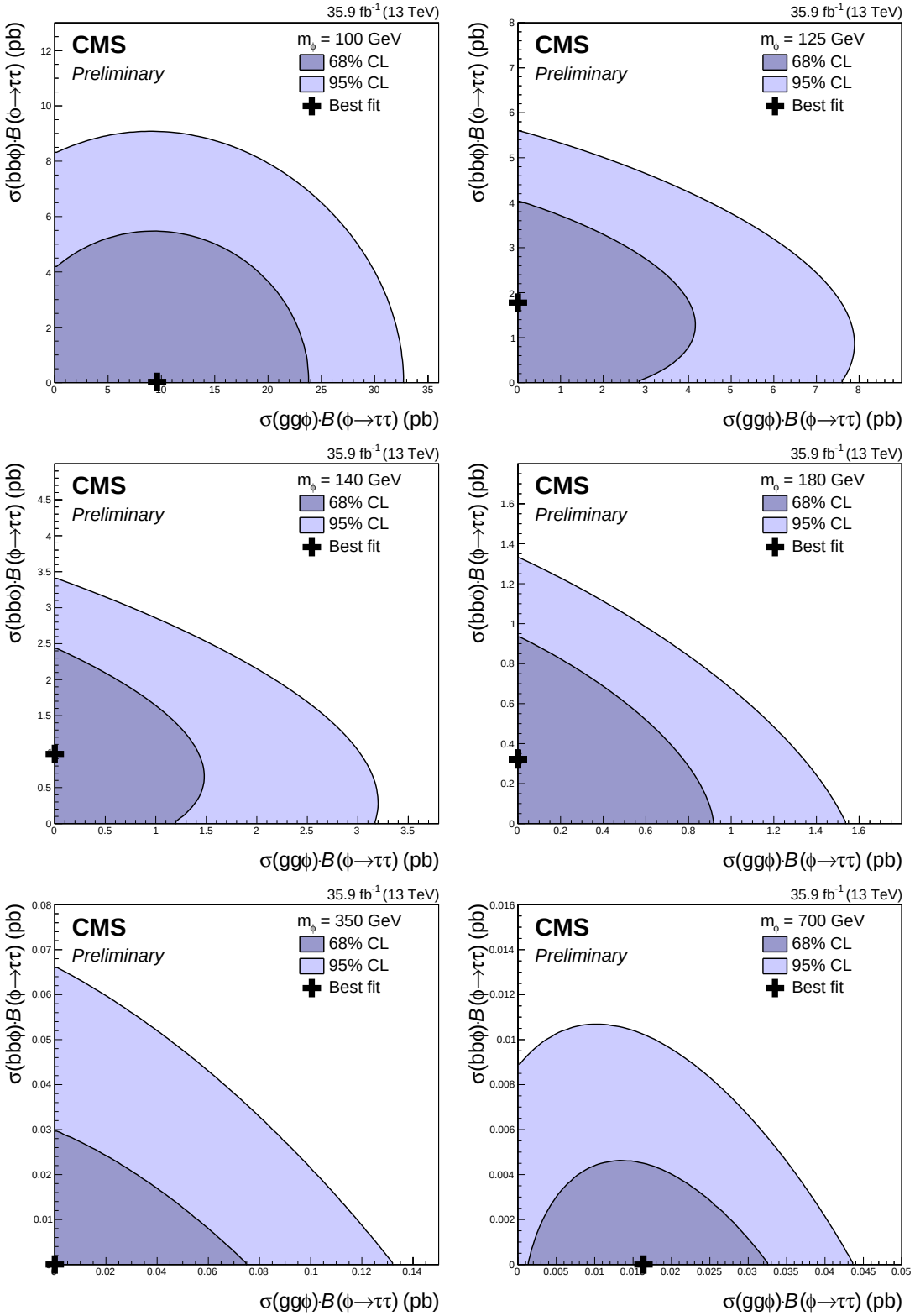

Figure 8: Scan of the likelihood function for the search in the di-τ final state for a single narrow resonance ϕ produced via gluon-fusion or in association with b quarks. A representative subset of the mass points tested at (upper left) 100 GeV, (upper right) 125 GeV, (middle left) 140 GeV, (middle right) 180 GeV, (lower left) 350 GeV and (lower right) 700 GeV is shown.

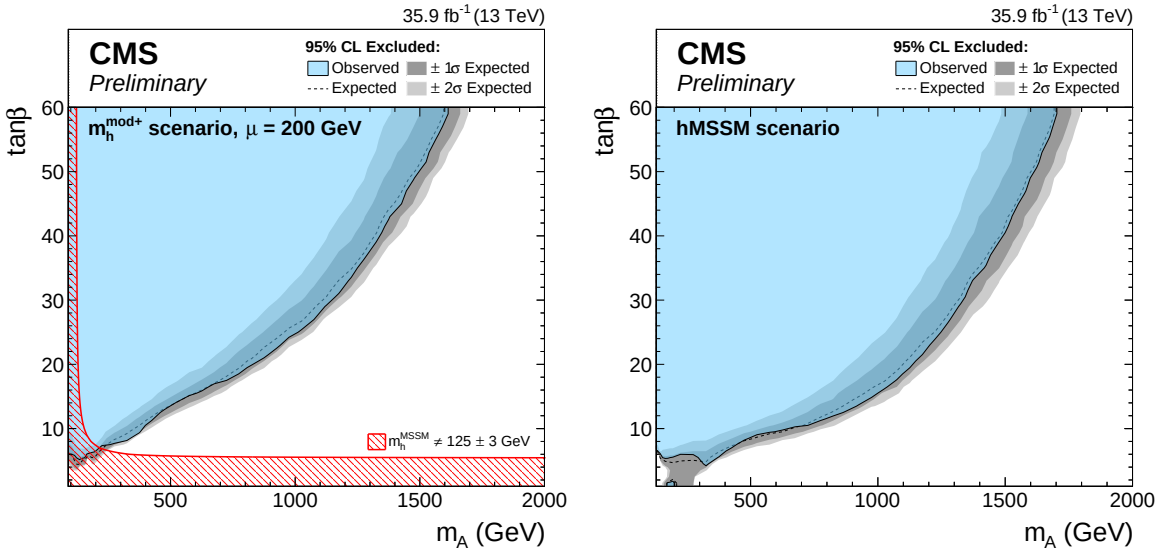

Figure 9: Expected and observed 95% CL exclusion contour (left) in the MSSM $m_{\mathrm{h}}^{\mathrm{mod+}}$ and (right) in the hMSSM scenario. The expected median is shown as a dashed black line. The dark and bright gray bands indicate the 68% and 95% confidence intervals for the variation of the expected exclusion. The observed exclusion contour is indicated by the colored blue area.

References

[1] ATLAS Collaboration, "Observation of a New Particle in the Search for the Standard Model Higgs Boson with the ATLAS Detector at the LHC", *Phys.Lett.* **B716** (2012) 1–29, doi:10.1016/j.physletb.2012.08.020, arXiv:1207.7214.

[2] CMS Collaboration, "Observation of a new boson at a mass of 125 GeV with the CMS experiment at the LHC", *Phys. Lett.* **B716** (2012) 30–61, doi:10.1016/j.physletb.2012.08.021, arXiv:1207.7235.

[3] CMS Collaboration, "Observation of a new boson with mass near 125 GeV in pp collisions at $\sqrt{s}$ = 7 and 8 TeV", *JHEP* **06** (2013) 081, doi:10.1007/JHEP06(2013)081, arXiv:1303.4571.

[4] P. W. Higgs, "Broken symmetries, massless particles and gauge fields", *Phys. Lett.* **12** (1964) 132–133, doi:10.1016/0031-9163(64)91136-9.

[5] P. W. Higgs, "Broken Symmetries and the Masses of Gauge Bosons", *Phys. Rev. Lett.* **13** (1964) 508–509, doi:10.1103/PhysRevLett.13.508.

[6] G. S. Guralnik, C. R. Hagen, and T. W. B. Kibble, "Global Conservation Laws and Massless Particles", *Phys. Rev. Lett.* **13** (1964) 585–587, doi:10.1103/PhysRevLett.13.585.

[7] P. W. Higgs, "Spontaneous Symmetry Breakdown without Massless Bosons", *Phys. Rev.* **145** (1966) 1156–1163, doi:10.1103/PhysRev.145.1156.

[8] T. W. B. Kibble, "Symmetry breaking in nonAbelian gauge theories", *Phys. Rev.* **155** (1967) 1554–1561, doi:10.1103/PhysRev.155.1554.

[9] F. Englert and R. Brout, "Broken Symmetry and the Mass of Gauge Vector Mesons", *Phys. Rev. Lett.* **13** (1964) 321–323, doi:10.1103/PhysRevLett.13.321.

[10] ATLAS, CMS Collaboration, "Combined Measurement of the Higgs Boson Mass in pp Collisions at $\sqrt{s} = 7$ and 8 TeV with the ATLAS and CMS Experiments", *Phys. Rev. Lett.* **114** (2015) 191803, doi:10.1103/PhysRevLett.114.191803, arXiv:1503.07589.

[11] ATLAS, CMS Collaboration, "Measurements of the Higgs boson production and decay rates and constraints on its couplings from a combined ATLAS and CMS analysis of the LHC pp collision data at $\sqrt{s} = 7$ and 8 TeV", *JHEP* **08** (2016) 045, doi:10.1007/JHEP08(2016)045, arXiv:1606.02266.

[12] Yu. A. Golfand and E. P. Likhtman, "Extension of the Algebra of Poincare Group Generators and Violation of p Invariance", *JETP Lett.* **13** (1971) 323–326. [Pisma Zh. Eksp. Teor. Fiz.13,452(1971)].

[13] J. Wess and B. Zumino, "Supergauge Transformations in Four-Dimensions", *Nucl. Phys.* **B70** (1974) 39–50, doi:10.1016/0550-3213(74)90355-1.

[14] P. Fayet, "Supergauge Invariant Extension of the Higgs Mechanism and a Model for the electron and Its Neutrino", *Nucl. Phys.* **B90** (1975) 104–124, doi:10.1016/0550-3213(75)90636-7.

[15] P. Fayet, "Spontaneously Broken Supersymmetric Theories of Weak, Electromagnetic and Strong Interactions", *Phys. Lett.* **69B** (1977) 489, doi:10.1016/0370-2693(77)90852-8.

[16] M. Carena et al., "MSSM Higgs Boson Searches at the LHC: Benchmark Scenarios after the Discovery of a Higgs-like Particle", *Eur. Phys. J.* **C73** (2013), no. 9, 2552, doi:10.1140/epjc/s10052-013-2552-1, arXiv:1302.7033.

[17] DELPHI, OPAL, ALEPH, LEP Working Group for Higgs Boson Searches, L3 Collaboration, "Search for neutral MSSM Higgs bosons at LEP", *Eur. Phys. J.* **C47** (2006) 547–587, doi:10.1140/epjc/s2006-02569-7, arXiv:hep-ex/0602042.

[18] CDF Collaboration, "Search for Higgs bosons predicted in two-Higgs-doublet models via decays to tau lepton pairs in 1.96-TeV p anti-p collisions", *Phys. Rev. Lett.* **103** (2009) 201801, doi:10.1103/PhysRevLett.103.201801, arXiv:0906.1014.

[19] D0 Collaboration, "Search for neutral Higgs bosons in the multi-b-jet topology in 5.2fb^{-1} of $p\bar{p}$ collisions at $\sqrt{s} = 1.96$ TeV", *Phys. Lett.* **B698** (2011) 97–104, doi:10.1016/j.physletb.2011.02.062, arXiv:1011.1931.

[20] D0 Collaboration, "Search for Higgs bosons decaying to $\tau\tau$ pairs in $p\bar{p}$ collisions at $\sqrt{s} = 1.96$ TeV", *Phys. Lett.* **B707** (2012) 323–329, doi:10.1016/j.physletb.2011.12.050, arXiv:1106.4555.

[21] CDF Collaboration, "Search for Higgs Bosons Produced in Association with b-quarks", *Phys. Rev.* **D85** (2012) 032005, doi:10.1103/PhysRevD.85.032005, arXiv:1106.4782.

[22] CMS Collaboration, "Search for a Higgs boson decaying into a b-quark pair and produced in association with b quarks in proton proton collisions at 7 TeV", *Phys. Lett.* **B722** (2013) 207–232, doi:10.1016/j.physletb.2013.04.017, arXiv:1302.2892.

[23] CMS Collaboration, "Search for neutral MSSM Higgs bosons decaying into a pair of bottom quarks", *JHEP* **11** (2015) 071, doi:10.1007/JHEP11(2015)071, arXiv:1506.08329.

[24] ATLAS Collaboration, "Search for the neutral Higgs bosons of the Minimal Supersymmetric Standard Model in pp collisions at $\sqrt{s} = 7$ TeV with the ATLAS detector", *JHEP* **02** (2013) 095, doi:10.1007/JHEP02(2013)095, arXiv:1211.6956.

[25] CMS Collaboration, "Search for neutral MSSM Higgs bosons decaying to $\mu^+\mu^-$ in pp collisions at $\sqrt{s} = 7$ and 8 TeV", *Phys. Lett.* **B752** (2016) 221–246, doi:10.1016/j.physletb.2015.11.042, arXiv:1508.01437.

[26] ATLAS Collaboration, "Search for neutral Higgs bosons of the minimal supersymmetric standard model in pp collisions at $\sqrt{s}$ = 8 TeV with the ATLAS detector", *JHEP* **11** (2014) 056, doi:10.1007/JHEP11(2014)056, arXiv:1409.6064.

[27] ATLAS Collaboration, "Search for Minimal Supersymmetric Standard Model Higgs bosons H/A and for a Z' boson in the $\tau\tau$ final state produced in pp collisions at $\sqrt{s} = 13$ TeV with the ATLAS Detector", *Eur. Phys. J.* **C76** (2016), no. 11, 585, doi:10.1140/epjc/s10052-016-4400-6, arXiv:1608.00890.

[28] CMS Collaboration, "Search for Neutral MSSM Higgs Bosons Decaying to Tau Pairs in pp Collisions at $\sqrt{s} = 7$ TeV", *Phys. Rev. Lett.* **106** (2011) 231801, doi:10.1103/PhysRevLett.106.231801, arXiv:1104.1619.

[29] CMS Collaboration, "Search for neutral Higgs bosons decaying to tau pairs in pp collisions at $\sqrt{s} = 7$ TeV", *Phys. Lett.* **B713** (2012) 68–90, doi:10.1016/j.physletb.2012.05.028, arXiv:1202.4083.

[30] CMS Collaboration, "Search for neutral MSSM Higgs bosons decaying to a pair of tau leptons in pp collisions", *JHEP* **10** (2014) 160, doi:10.1007/JHEP10(2014)160, arXiv:1408.3316.

[31] CMS Collaboration, "Description and performance of track and primary-vertex reconstruction with the CMS tracker", *JINST* **9** (2014) P10009, doi:10.1088/1748-0221/9/10/P10009, arXiv:1405.6569.

[32] CMS Collaboration, "Performance of photon reconstruction and identification with the CMS detector in proton-proton collisions at $\sqrt{s} = 8$ TeV", *JINST* **10** (2015) P08010, doi:10.1088/1748-0221/10/08/P08010, arXiv:1502.02702.

[33] CMS Collaboration, "Performance of Electron Reconstruction and Selection with the CMS Detector in Proton-Proton Collisions at s = 8 TeV", *JINST* **10** (2015), no. 06, P06005, doi:10.1088/1748-0221/10/06/P06005, arXiv:1502.02701.

[34] CMS Collaboration, "Performance of CMS muon reconstruction in pp collision events at $\sqrt{s} = 7$ TeV", *JINST* **7** (2012) P10002, doi:10.1088/1748-0221/7/10/P10002, arXiv:1206.4071.

[35] CMS Collaboration, "The CMS trigger system", *JINST* **12** (2017) P01020, doi:10.1088/1748-0221/12/01/P01020, arXiv:1609.02366.

[36] CMS Collaboration, "The CMS experiment at the CERN LHC", *JINST* **3** (2008) S08004, doi:10.1088/1748-0221/3/08/S08004.

[37] CMS Collaboration, "Particle-flow reconstruction and global event description with the CMS detector", *JINST* **12** (2017), no. 10, P10003, doi:10.1088/1748-0221/12/10/P10003, arXiv:1706.04965.

[38] K. Rose, "Deterministic annealing for clustering, compression, classification, regression, and related optimization problems", *Proceedings of the IEEE* **86** (Nov, 1998) 2210–2239, doi:10.1109/5.726788.

[39] H. Voss, A. Höcker, J. Stelzer, and F. Tegenfeldt, "TMVA, the Toolkit for Multivariate Data Analysis with ROOT", in *XIth International Workshop on Advanced Computing and Analysis Techniques in Physics Research (ACAT)*, p. 40. 2007. arXiv:physics/0703039.

[40] M. Cacciari, G. P. Salam, and G. Soyez, "FastJet user manual", *Eur. Phys. J. C* **72** (2012) 1896, doi:10.1140/epjc/s10052-012-1896-2, arXiv:1111.6097.

[41] CMS Collaboration, "Identification of b-quark jets with the CMS experiment", *JINST* **8** (2013) P04013, doi:10.1088/1748-0221/8/04/P04013, arXiv:1211.4462.

[42] CMS Collaboration, "Reconstruction and identification of τ lepton decays to hadrons and τ_ν at CMS", *JINST* **11** (2016), no. 01, P01019, doi:10.1088/1748-0221/11/01/P01019, arXiv:1510.07488.

[43] CMS Collaboration, "Performance of reconstruction and identification of tau leptons in their decays to hadrons and tau neutrino in LHC Run-2", Technical Report CMS-PAS-TAU-16-002, CERN, Geneva, 2016.

[44] J. Alwall et al., "MadGraph 5 : Going Beyond", *JHEP* **06** (2011) 128, doi:10.1007/JHEP06(2011)128, arXiv:1106.0522.

[45] J. Alwall et al., "The automated computation of tree-level and next-to-leading order differential cross sections, and their matching to parton shower simulations", *JHEP* **07** (2014) 079, doi:10.1007/JHEP07(2014)079, arXiv:1405.0301.

[46] P. Nason, "A New method for combining NLO QCD with shower Monte Carlo algorithms", *JHEP* **11** (2004) 040, doi:10.1088/1126-6708/2004/11/040, arXiv:hep-ph/0409146.

[47] S. Frixione, P. Nason, and C. Oleari, "Matching NLO QCD computations with Parton Shower simulations: the POWHEG method", *JHEP* **11** (2007) 070, doi:10.1088/1126-6708/2007/11/070, arXiv:0709.2092.

[48] S. Alioli, P. Nason, C. Oleari, and E. Re, "NLO Higgs boson production via gluon fusion matched with shower in POWHEG", *JHEP* **04** (2009) 002, doi:10.1088/1126-6708/2009/04/002, arXiv:0812.0578.

[49] S. Alioli, P. Nason, C. Oleari, and E. Re, "A general framework for implementing NLO calculations in shower Monte Carlo programs: the POWHEG BOX", *JHEP* **06** (2010) 043, doi:10.1007/JHEP06(2010)043, arXiv:1002.2581.

[50] S. Alioli et al., "Jet pair production in POWHEG", *JHEP* **04** (2011) 081, doi:10.1007/JHEP04(2011)081, arXiv:1012.3380.

[51] E. Bagnaschi, G. Degrassi, P. Slavich, and A. Vicini, "Higgs production via gluon fusion in the POWHEG approach in the SM and in the MSSM", *JHEP* **02** (2012) 088, doi:10.1007/JHEP02(2012)088, arXiv:1111.2854.

[52] K. Melnikov and F. Petriello, "Electroweak gauge boson production at hadron colliders through O(alpha(s)**2)", *Phys. Rev.* **D74** (2006) 114017, doi:10.1103/PhysRevD.74.114017, arXiv:hep-ph/0609070.

[53] N. Kidonakis, "Top Quark Production", in *Proceedings, Helmholtz International Summer School on Physics of Heavy Quarks and Hadrons (HQ 2013): JINR, Dubna, Russia, July 15-28, 2013*, pp. 139–168. 2014. arXiv:1311.0283. doi:10.3204/DESY-PROC-2013-03/Kidonakis.

[54] J. M. Campbell and R. K. Ellis, "MCFM for the Tevatron and the LHC", *Nucl. Phys. Proc. Suppl.* **205-206** (2010) 10–15, doi:10.1016/j.nuclphysbps.2010.08.011, arXiv:1007.3492.

[55] T. Sjostrand, S. Mrenna, and P. Z. Skands, "A Brief Introduction to PYTHIA 8.1", *Comput. Phys. Commun.* **178** (2008) 852–867, doi:10.1016/j.cpc.2008.01.036, arXiv:0710.3820.

[56] E. Bagnaschi et al., "Resummation ambiguities in the Higgs transverse-momentum spectrum in the Standard Model and beyond", *JHEP* **01** (2016) 090, doi:10.1007/JHEP01(2016)090, arXiv:1510.08850.

[57] E. Bagnaschi and A. Vicini, "The Higgs transverse momentum distribution in gluon fusion as a multiscale problem", *JHEP* **01** (2016) 056, doi:10.1007/JHEP01(2016)056, arXiv:1505.00735.

[58] R. V. Harlander, H. Mantler, and M. Wiesemann, "Transverse momentum resummation for Higgs production via gluon fusion in the MSSM", *JHEP* **11** (2014) 116, doi:10.1007/JHEP11(2014)116, arXiv:1409.0531.

[59] NNPDF Collaboration, "Unbiased global determination of parton distributions and their uncertainties at NNLO and at LO", *Nucl. Phys.* **B855** (2012) 153–221, doi:10.1016/j.nuclphysb.2011.09.024, arXiv:1107.2652.

[60] CMS Collaboration, "Event generator tunes obtained from underlying event and multiparton scattering measurements", *Eur. Phys. J.* **C76** (2016), no. 3, 155, doi:10.1140/epjc/s10052-016-3988-x, arXiv:1512.00815.

[61] S. Agostinelli et al., "G4–a simulation toolkit", *Nuclear Instruments and Methods in Physics Research Section A: Accelerators, Spectrometers, Detectors and Associated Equ ipment* **506** (2003), no. 3, 250 – 303, doi:10.1016/S0168-9002(03)01368-8.

[62] CMS Collaboration, "Measurements of Inclusive W and Z Cross Sections in pp Collisions at $\sqrt{s} = 7$ TeV", *JHEP* **01** (2011) 080, doi:10.1007/JHEP01(2011)080, arXiv:1012.2466.

[63] CMS Collaboration, "Measurement of the differential cross section for top quark pair production in pp collisions at $\sqrt{s} = 8$ TeV", *Eur. Phys. J.* **C75** (2015), no. 11, 542, doi:10.1140/epjc/s10052-015-3709-x, arXiv:1505.04480.

[64] CMS Collaboration, "Evidence for the 125 GeV Higgs boson decaying to a pair of τ leptons", *JHEP* **05** (2014) 104, doi:10.1007/JHEP05(2014)104, arXiv:1401.5041.

[65] ATLAS Collaboration, "Modelling $Z \to \tau\tau$ processes in ATLAS with τ-embedded $Z \to \mu\mu$ data", *JINST* **10** (2015), no. 09, P09018, doi:10.1088/1748-0221/10/09/P09018, 10.1088/1748-0221/2015/9/P09018, arXiv:1506.05623.

[66] A. L. Read, "Linear interpolation of histograms", *Nucl. Instrum. Meth.* **A425** (1999) 357–360, doi:10.1016/S0168-9002(98)01347-3.

[67] CMS Collaboration, "CMS Luminosity Measurements for the 2016 Data Taking Period", Technical Report CMS-PAS-LUM-17-001, CERN, Geneva, 2017.

[68] LHC Higgs Cross Section Working Group Collaboration, "Handbook of LHC Higgs Cross Sections: 4. Deciphering the Nature of the Higgs Sector", doi:10.23731/CYRM-2017-002, arXiv:1610.07922.

[69] A. D. Martin, W. J. Stirling, R. S. Thorne, and G. Watt, "Parton distributions for the LHC", *Eur. Phys. J.* **C63** (2009) 189–285, doi:10.1140/epjc/s10052-009-1072-5, arXiv:0901.0002.

[70] A. D. Martin, W. J. Stirling, R. S. Thorne, and G. Watt, "Uncertainties on alpha(S) in global PDF analyses and implications for predicted hadronic cross sections", *Eur. Phys. J.* **C64** (2009) 653–680, doi:10.1140/epjc/s10052-009-1164-2, arXiv:0905.3531.

[71] T. Junk, "Confidence level computation for combining searches with small statistics", *Nucl. Instrum. Meth.* **A434** (1999) 435–443, doi:10.1016/S0168-9002(99)00498-2, arXiv:hep-ex/9902006.

[72] A. L. Read, "Presentation of search results: The CL(s) technique", *J. Phys.* **G28** (2002) 2693–2704, doi:10.1088/0954-3899/28/10/313. [,11(2002)].

[73] The ATLAS Collaboration, The CMS Collaboration, The LHC Higgs Combination Group Collaboration, "Procedure for the LHC Higgs boson search combination in Summer 2011", Technical Report CMS-NOTE-2011-005. ATL-PHYS-PUB-2011-11, CERN, Geneva, Aug, 2011.

[74] CMS Collaboration, "Combined results of searches for the standard model Higgs boson in pp collisions at $\sqrt{s} = 7$ TeV", *Phys. Lett.* **B710** (2012) 26–48, doi:10.1016/j.physletb.2012.02.064, arXiv:1202.1488.

[75] L. Maiani, A. D. Polosa, and V. Riquer, "Bounds to the Higgs Sector Masses in Minimal Supersymmetry from LHC Data", *Phys. Lett.* **B724** (2013) 274–277, doi:10.1016/j.physletb.2013.06.026, arXiv:1305.2172.

[76] A. Djouadi et al., "The post-Higgs MSSM scenario: Habemus MSSM?", *Eur. Phys. J.* **C73** (2013) 2650, doi:10.1140/epjc/s10052-013-2650-0, arXiv:1307.5205.

[77] A. Djouadi et al., "Fully covering the MSSM Higgs sector at the LHC", *JHEP* **06** (2015) 168, doi:10.1007/JHEP06(2015)168, arXiv:1502.05653.

[78] G. Degrassi et al., "Towards high precision predictions for the MSSM Higgs sector", *Eur. Phys. J. C* **28** (2003) 133–143, doi:10.1140/epjc/s2003-01152-2, arXiv:hep-ph/0212020.

[79] B. C. Allanach et al., "Precise determination of the neutral Higgs boson masses in the MSSM", *JHEP* **09** (2004) 044, doi:10.1088/1126-6708/2004/09/044, arXiv:hep-ph/0406166.

[80] LHC Higgs Cross Section Working Group Collaboration, "Handbook of LHC Higgs Cross Sections: 3. Higgs Properties", doi:10.5170/CERN-2013-004, arXiv:1307.1347.

[81] R. V. Harlander, S. Liebler, and H. Mantler, "SusHi: A program for the calculation of Higgs production in gluon fusion and bottom-quark annihilation in the Standard Model and the MSSM", *Comput. Phys. Commun.* **184** (2013) 1605–1617, doi:10.1016/j.cpc.2013.02.006, arXiv:1212.3249.

[82] M. Spira, A. Djouadi, D. Graudenz, and P. M. Zerwas, "Higgs boson production at the LHC", *Nucl. Phys.* **B453** (1995) 17–82, doi:10.1016/0550-3213(95)00379-7, arXiv:hep-ph/9504378.

[83] R. V. Harlander and M. Steinhauser, "Supersymmetric Higgs production in gluon fusion at next-to-leading order", *JHEP* **09** (2004) 066, doi:10.1088/1126-6708/2004/09/066, arXiv:hep-ph/0409010.

[84] R. Harlander and P. Kant, "Higgs production and decay: Analytic results at next-to-leading order QCD", *JHEP* **12** (2005) 015, doi:10.1088/1126-6708/2005/12/015, arXiv:hep-ph/0509189.

[85] G. Degrassi and P. Slavich, "NLO QCD bottom corrections to Higgs boson production in the MSSM", *JHEP* **11** (2010) 044, doi:10.1007/JHEP11(2010)044, arXiv:1007.3465.

[86] G. Degrassi, S. Di Vita, and P. Slavich, "NLO QCD corrections to pseudoscalar Higgs production in the MSSM", *JHEP* **08** (2011) 128, doi:10.1007/JHEP08(2011)128, arXiv:1107.0914.

[87] G. Degrassi, S. Di Vita, and P. Slavich, "On the NLO QCD Corrections to the Production of the Heaviest Neutral Higgs Scalar in the MSSM", *Eur. Phys. J.* **C72** (2012) 2032, doi:10.1140/epjc/s10052-012-2032-z, arXiv:1204.1016.

[88] R. V. Harlander and W. B. Kilgore, "Next-to-next-to-leading order Higgs production at hadron colliders", *Phys. Rev. Lett.* **88** (2002) 201801, doi:10.1103/PhysRevLett.88.201801, arXiv:hep-ph/0201206.

[89] C. Anastasiou and K. Melnikov, "Higgs boson production at hadron colliders in NNLO QCD", *Nucl. Phys.* **B646** (2002) 220–256, doi:10.1016/S0550-3213(02)00837-4, arXiv:hep-ph/0207004.

[90] V. Ravindran, J. Smith, and W. L. van Neerven, "NNLO corrections to the total cross-section for Higgs boson production in hadron hadron collisions", *Nucl. Phys.* **B665** (2003) 325–366, doi:10.1016/S0550-3213(03)00457-7, arXiv:hep-ph/0302135.

[91] R. V. Harlander and W. B. Kilgore, "Production of a pseudoscalar Higgs boson at hadron colliders at next-to-next-to leading order", *JHEP* **10** (2002) 017, doi:10.1088/1126-6708/2002/10/017, arXiv:hep-ph/0208096.

[92] C. Anastasiou and K. Melnikov, "Pseudoscalar Higgs boson production at hadron colliders in NNLO QCD", *Phys. Rev.* **D67** (2003) 037501, doi:10.1103/PhysRevD.67.037501, arXiv:hep-ph/0208115.

[93] U. Aglietti, R. Bonciani, G. Degrassi, and A. Vicini, "Two loop light fermion contribution to Higgs production and decays", *Phys. Lett.* **B595** (2004) 432–441, doi:10.1016/j.physletb.2004.06.063, arXiv:hep-ph/0404071.

[94] R. Bonciani, G. Degrassi, and A. Vicini, "On the Generalized Harmonic Polylogarithms of One Complex Variable", *Comput. Phys. Commun.* **182** (2011) 1253–1264, doi:10.1016/j.cpc.2011.02.011, arXiv:1007.1891.

[95] S. Dittmaier, M. Kramer, 1, and M. Spira, "Higgs radiation off bottom quarks at the Tevatron and the CERN LHC", *Phys. Rev. D* **70** (2004) 074010, doi:10.1103/PhysRevD.70.074010, arXiv:hep-ph/0309204.

[96] S. Dawson, C. B. Jackson, L. Reina, and D. Wackeroth, "Exclusive higgs boson production with bottom quarks at hadron colliders", *Phys. Rev. D* **69** (Apr, 2004) 074027, doi:10.1103/PhysRevD.69.074027.

[97] R. V. Harlander and W. B. Kilgore, "Higgs boson production in bottom quark fusion at next-to-next-to-leading order", *Phys. Rev. D* **68** (Jul, 2003) 013001, doi:10.1103/PhysRevD.68.013001.

[98] R. Harlander, M. Kramer, and M. Schumacher, "Bottom-quark associated Higgs-boson production: reconciling the four- and five-flavour scheme approach", arXiv:1112.3478.

[99] S. Heinemeyer, W. Hollik, and G. Weiglein, "FeynHiggs: A Program for the calculation of the masses of the neutral CP even Higgs bosons in the MSSM", *Comput. Phys. Commun.* **124** (2000) 76–89, doi:10.1016/S0010-4655(99)00364-1, arXiv:hep-ph/9812320.

[100] S. Heinemeyer, W. Hollik, and G. Weiglein, "The Masses of the neutral CP - even Higgs bosons in the MSSM: Accurate analysis at the two loop level", *Eur. Phys. J. C* **9** (1999) 343–366, doi:10.1007/s100529900006,10.1007/s100520050537, arXiv:hep-ph/9812472.

[101] M. Frank et al., "The Higgs Boson Masses and Mixings of the Complex MSSM in the Feynman-Diagrammatic Approach", *JHEP* **02** (2007) 047, doi:10.1088/1126-6708/2007/02/047,arXiv:hep-ph/0611326.

[102] T. Hahn et al., "High-Precision Predictions for the Light CP -Even Higgs Boson Mass of the Minimal Supersymmetric Standard Model", *Phys. Rev. Lett.* **112** (2014), no. 14, 141801, doi:10.1103/PhysRevLett.112.141801,arXiv:1312.4937.

[103] A. Djouadi, J. Kalinowski, and M. Spira, "HDECAY: A Program for Higgs boson decays in the standard model and its supersymmetric extension", *Comput. Phys. Commun.* **108** (1998) 56–74, doi:10.1016/S0010-4655(97)00123-9,arXiv:hep-ph/9704448.